Pattern formation in a nonlocal mathematical model for the multiple roles of the TGF- pathway in tumour dynamics

Eftimie, Raluca; Perez, Matthieu ; Buono, Pietro-Luciano

Published in:
Mathematical Biosciences

DOI:
10.1016/j.mbs.2017.05.003

Publication date:
2017

Document Version
Peer reviewed version

Link to Final Version: https://doi.org/10.1016/j.mbs.2017.05.003

Pattern formation in a nonlocal mathematical model for the multiple roles of the TGF-β pathway in tumour dynamics

Raluca Eftimie[a,*], Matthieu Perez[b], Pietro-Luciano Buono[c]

[a] *Division of Mathematics, University of Dundee, Dundee, DD1 4HN, United Kingdom*
[b] *Institut National Des Sciences Appliquees de Rouen, 76801 Saint Etienne du Rouvray Cedex, France*
[c] *Faculty of Science, University of Ontario Institute of Technology, Oshawa, Ontario, L1H 7K4, Canada*

Abstract

The growth and invasion of cancer cells are very complex processes, which can be regulated by the cross-talk between various signalling pathways, or by single signalling pathways that can control multiple aspects of cell behaviour. TGF-β is one of the most investigated signalling pathways in oncology, since it can regulate multiple aspects of cell behaviour: cell proliferation and apoptosis, cell-cell adhesion and epithelial-to-mesenchimal transition via loss of cell adhesion. In this study, we use a mathematical modelling approach to investigate the complex roles of TGF-β signalling pathways on the inhibition and growth of tumours, as well as on the epithelial-to-mesenchimal transition involved in the metastasis of tumour cells. We show that the nonlocal mathematical model derived here to describe repulsive and adhesive cell-cell interactions can explain the formation of new tumour cell aggregations at positions in space that are further away from the main aggregation. Moreover, we show that the increase in cell-cell adhesion leads to fewer but larger aggregations, and the increase in TGF-β molecules – whose late-stage effect is to decrease cell adhesion – leads to many small cellular aggregations. Finally, we perform a sensitivity analysis on some parameters associated with TGF-β dynamics, and use it to investigate the relation between the tumour size and its metastatic spread.

Keywords: nonlocal spatial mathematical model, tumour invasion, TGF-β
2010 MSC: 92-08, 92C15, 92C17, 92C50

*Corresponding author
Email address: r.a.eftimie@dundee.ac.uk (Raluca Eftimie)

1. Introduction

Understanding and controlling the factors that govern the evolution of solid tumours has been one of the main research directions in cell biology for at least a century [1]. One of the most poorly understood aspects associated with tumour progression is tissue invasion and metastasis, a process that allows for cells to escape the primary tumour and to colonise new tissues [2, 3]. This very complex process is generally regulated by a cross-talk between multiple signalling pathways [4, 5, 6]. Moreover, some of these pathways are controlling multiple aspects of cell behaviour. Among the most investigated signalling pathways is the TGF-β pathway, which is involved in cell proliferation and apoptosis, cell-cell adhesion, cell motility, cell differentiation, immune response [7]; see also Figure 1(a). The expression of this pathway has been studied in the majority of epithelial cancers: from prostate cancer, to skin, breast, lung, colorectal, and pancreatic cancers [7, 8]. Moreover, experimental studies have shown that TGF-β has a dual cancer role: in many early-stage tumours TGF-β has an anti-tumour effect, while in advanced tumours the TGF-β pathway is disregulated and promotes tumour growth and metastasis [7]. However, the timing at which TGF-β role switches from tumour-suppressor to tumour-inhibitor is still unclear [9]; see also Figure 2). A particular aspect of the metastasis process, which has been shown to be influenced by the TGF-β pathway, is the epithelial-to-mesenchimal transition (EMT) [10]. During EMT, the E-cadherin proteins involved in cell-cell adhesion are down-regulated in the presence of TGF-β molecules, and the epithelial cells loose cell-cell junction integrity and invade new tissues [10, 8]; see also Figure 1. The overall complexity of this pathway in shown in the contradictory results associated with cancer treatment: while many studies suggest the inhibition of TGF-β pathway to improve cancer treatments [11], other studies have shown that TGF-β inhibition can increase inflammation and accelerate pre-neoplastic lesions which were still controlled by TGF-β [12, 9].

The detailed dynamics of the molecular components of the TGF-β signalling pathway has been investigated by various mathematical models [13, 14, 15]. Many other mathematical models focused on the TGF-β role in the evolution of cancer. For example, Chung et al. [14] developed an ODE model for the dynamics of the components of the TGF-β/Smad signalling pathway, and used it to describe the TGF-β dose-dependent responses for these various molecular components in the presence of cancer cells. Ascolani et al. [16] derived models for the molecular and cellular mechanisms behind TGF-β role in tumour suppression or tumour progression (again, with a focus on the molecular components of the TGF-β pathway, the concentration of TGF-β molecules, the density of some cell population and the TGF-β receptors on cell membranes). Arciero et al., [17] ignored the detailed molecular dynamics of the TGF-β pathway and focused on cell-level immune suppressive and tumour promoting effects of TGF-β. Kim and Othmer [18] derived a complex hybrid model to investigate the role of TGF-β/EGF pathways on the spatial growth of fibroblasts/myofibroblasts in tumour stromal tissue (where the intra-cellular dynamics of the signalling pathway was described by ODEs, the dynamics of TGF-β and EGF molecules in the

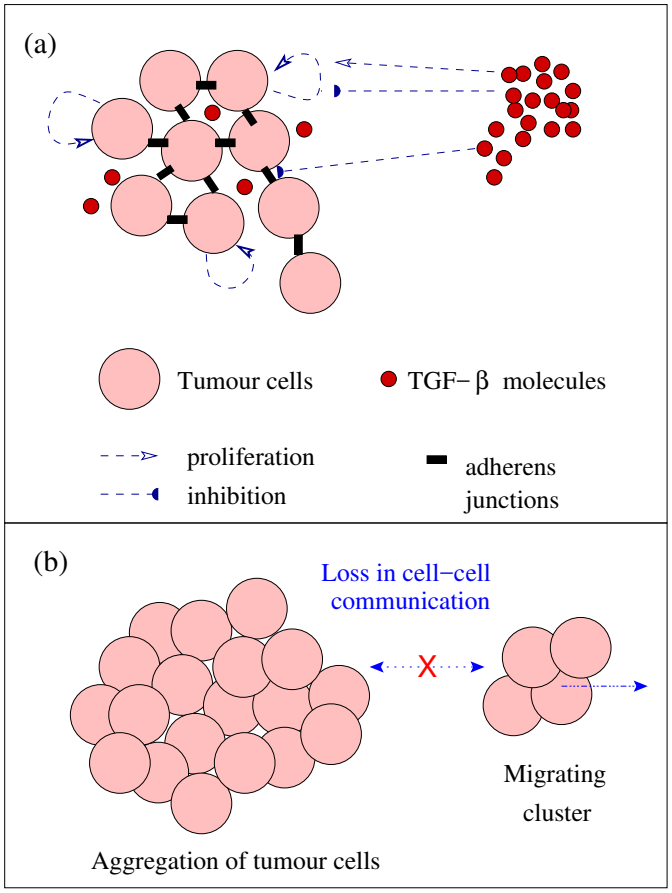

Figure 1: (a) Caricature description of the dynamics of tumour cells, and the interactions with the TGF-β molecules. (b) Caricature description of the metastasis process, where a cell or a cluster of cells breaks off from the main tumour cell aggregation and migrate to distant places.

stromal tissue was described by reaction-diffusion equations, and the growth and movement of the tumour was described by a particle-based model). Finally, Wang et al. [19] considered a local Fisher-Kolmogorov equation to model the spatial dynamics of tumour cells in response to TGF-β molecules. However, these authors never modelled explicitly the effect of TGF-β on cell motility and growth; they only assumed that the presence of TGF-β would lead to changes in the constant random cell motility and constant tumour growth rate, and used experimental data to find values for these constants.

Despite these different mathematical approaches to investigate the various roles of TGF-β pathway on tumour dynamics, there are currently no mathematical models that investigate all these aspects (i.e., effect of TGF-β on growth/apoptosis of tumour cells, cell-cell and/or cell-matrix adhesion, and cell

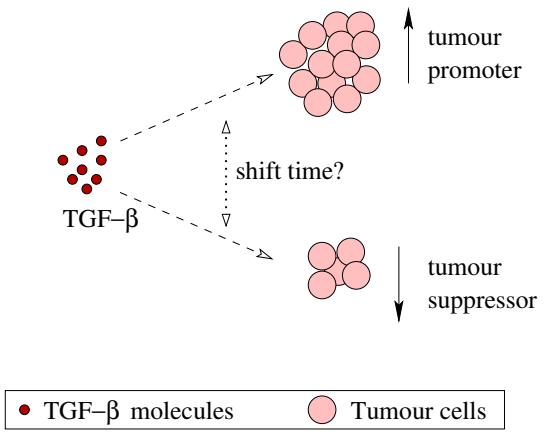

Figure 2: Dual role of TGF-β molecules on tumour dynamics: tumour suppressor and tumour promoter roles. Moreover, the timing for the switch from a tumour-suppressor to a tumour-promoter effect of TGF-β is still unclear [9].

invasion) in an unitary manner.

The aim of this study is to use a mathematical model to investigate the previously-identified multi-faceted role of TGF-β on tumour dynamics (see also Figure 1(b)). To this end, we use a system of nonlocal hyperbolic equations to describe the spatial movement of tumour cells (including their random and directed motion [20] as a result of random and directed turning behaviour), and their growth and decay in the presence of TGF-β molecules. We then couple this system with a local reaction-diffusion equation for the dynamics of TGF-β molecules. We first focus on the symmetry of the system and investigate the long-term dynamics of the model via steady state and stability analysis. We then use numerical simulations to show that the model can exhibit the formation of new cell aggregations at spatial positions further away from the original aggregations. In addition, we perform local sensitivity analysis to investigate the effect of small changes in the parameters that control the interactions between TGF-β molecules and tumour cells, on the overall tumour size and motility.

The article is structured as follows. In Section 2 we describe the mathematical model. In Section 3.3 we investigate the long-term behaviour of the system by focusing on the spatial homogeneous steady states and their symmetry. Then, in Section 4 we perform numerical simulations of the mathematical model, and investigate the sensitivity of tumour growth to changes in the parameters controlling TGF-β dynamics. We conclude with a summary and discussion of the results in Section 5.

2. Model description

To investigate the complex role of TGF-β molecules on tumour dynamics, we focus only on the densities of tumour cells, u_T, and the concentration of

TGF-β molecules, u_β. Moreover, to investigate the formation/break-up of tumour aggregations in response of TGF-β, as well as their migration, we focus on a domain that represents some tissue containing the tumour. For simplicity, throughout this study we consider a 1D domain. (A 2D generalisation of the model can be found in Appendix A.) To capture the polarity of cells during movement, we model separately the dynamics of left-moving u_T^- and right-moving u_T^+ tumour cells (where $u_T = u_T^+ + u_T^-$ is the total tumour cell density). The following equations describe the interactions between tumour cells and TGF-β molecules (u_β).

$$\begin{aligned}
\frac{\partial u_T^+}{\partial t} + \gamma \frac{\partial u_T^+}{\partial x} =& -\lambda^+[u_T, u_\beta]u_T^+ + \lambda^-[u_T, u_\beta]u_T^- \\
&+ \frac{1}{2} p_T u_T \Big(1 - \frac{u_T}{K_T}\Big) - \delta_T u_T^+ u_\beta (K_T^* - u_T), \qquad (1a)\\
\frac{\partial u_T^-}{\partial t} - \gamma \frac{\partial u_T^-}{\partial x} =& \lambda^+[u_T, u_\beta]u_T^+ - \lambda^-[u_T, u_\beta]u_T^- \\
&+ \frac{1}{2} p_T u_T \Big(1 - \frac{u_T}{K_T}\Big) - \delta_T u_T^- u_\beta (K_T^* - u_T), \qquad (1b)\\
\frac{\partial u_\beta}{\partial t} =& D \frac{\partial^2 u_\beta}{\partial x^2} + p_e + p_\beta u_T - \delta_\beta u_\beta. \qquad (1c)
\end{aligned}$$

Next, we describe in detail the various terms that appear in model (1).

1. *The tumour cells* move with velocity γ (fixed throughout this study), and change their movement directions from right-to-left or from left-to-right with rates λ^+ and λ^-, respectively. These turning rates depend on the attractive ($y_a^\pm$) and repulsive ($y_r^\pm$) interactions with other tumour cells, as well as on the TGF-β concentrations (u_β):

$$\lambda^\pm[u_T, u_\beta] = \lambda_1 + \lambda_2 f\left(y_r^\pm[u_T] - y_a^\pm[u_T, u_\beta]\right), \qquad (2)$$

Here λ_1 approximates the random turning, while $\lambda_2 f(\cdot)$ approximates the directed turning. Since cell turning cannot occur infinitely fast, we choose the turning function f to be a non-negative, bounded functional of the attractive-repulsive interactions ($y_{r,a}^\pm$) with neighbouring cells and chemical concentrations:

$$f(y_r^\pm - y_a^\pm) = 0.5 + 0.5 \tanh\left(y_r^\pm - y_a^\pm - m_0\right), \qquad (3)$$

where the term m_0 was chosen such that $f \approx 0$ when $y_r^\pm \approx y_a^\pm$ (see Table 2 and Figure 3(a), where $m_0 = 2$). We assume here that cells turn towards/away to/from other cells as a result of the attractive (i.e., adhesive) interactions [21] and repulsive interactions [22]; see also Fig. 4.

These interactions can be described by the following nonlocal terms:

$$y_r^{\pm}[u_T] = \pm\, q_r \int_0^{\infty} K_r(s)\Big(\mathbf{u_T}(\mathbf{x}+\mathbf{s}) - \mathbf{u_T}(\mathbf{x}-\mathbf{s})\Big)ds \tag{4a}$$

$$y_a^{\pm}[u_T, u_\beta] = \pm\, q_a \int_0^{\infty} K_a(s)\Big(\frac{\mathbf{u_T}(\mathbf{x}+\mathbf{s})}{k_\beta + u_\beta(x+s)} - \frac{\mathbf{u_T}(\mathbf{x}-\mathbf{s})}{k_\beta + u_\beta(x-s)}\Big)ds. \tag{4b}$$

As mentioned before, $u_T = u_T^+ + u_T^-$ is the total cell density. Parameters q_r and q_a represent the magnitudes of the repulsive and attractive (adhesive) interactions, respectively. The interaction kernels $K_r(s)$ and $K_a(s)$ describe the spatial ranges of these interactions, and an example of such kernels is depicted in Figure 3(b), for $s \geq 0$. (Note that we define the integrals in $y_{r,a}^{\pm}$ only for $s > 0$, and understand that a reference cell at x interacts only with those neighbours ahead at $x+s$, and behind at $x-s$, positioned within the repulsion/attraction ranges defined by $K_{r,a}(s) \gg 0$.) Equation (4a) incorporates the assumption that cell-cell repulsion is only the result of interactions with other neighbouring cells within the repulsion range. In particular, a reference cell at position x (i.e., $u_T^{\pm}(x,t)$) can detect - through mechanical traction stresses of neighbouring cells [23] - how many other cells are ahead/behind its spatial position (i.e., by calculating $u_T(x+s,t) - u_T(x-s,t)$, where $u_T = u_T^+ + u_T^-$). Moreover, we assume that the cell will change its polarisation towards the spatial region with lower cell density (i.e., the cell tries to avoid collision with higher densities of neighbouring cells). Equation (4b) incorporates also the assumption that the attractive cell-cell interactions are weakened by the presence of TGF-β molecules in the tumour microenvironment (at positions $x \pm s$ in space, where neighbouring cells are detected). These molecules decrease the E-cadherin expression on tumour cells leading to a loss in cell-cell adhesion [8]. We assumed here that only the TGF-β levels at cell boundaries $x \pm s$ (where a cell interacts with another cell) are important for cell-cell adhesion; local (at x) TGF-β levels could affect only cell-cell repulsion, but we are ignoring this aspect to focus exclusively on this cytokine's effect on cell adhesion. Finally, note that the terms $y_r^{\pm}$ and $y_a^{\pm}$ enter equation (3) with opposite signs, to depict that repulsion and attraction have opposite effects on the turning behaviour of cells.

In addition to movement and turning behaviours, tumour cells exhibit also a proliferative behaviour at a rate p_T, until they reach the carrying capacity K_T. Following the approach in [27] (for reaction-hyperbolic systems), we assume that there is equal probability of left-moving and right-moving cells to proliferate, and thus the proliferation terms in (1a)-(1b) are similar. Moreover, we assume that small tumours (i.e., $u_T < K_T^* = K_T/10^2$, with K_T^* a threshold parameter) have their growth inhibited by TGF-β molecules that act as a tumour suppressor. We denote this inhibition rate by δ_T. As tumour grows (i.e., $u_T > K_T^*$), the TGF-β undergoes a shift from a tumour-suppressing to a tumour-promoting molecule, and so δ_T

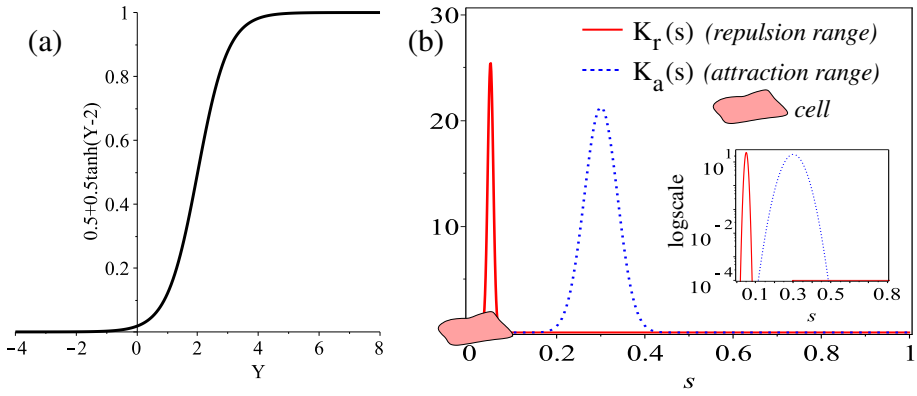

Figure 3: (a) Description of a nonnegative and bounded turning function $f(Y) = 0.5 + 0.5\tanh(Y - m_0)$, for $m_0 = 2$; (b) Example of translated Gaussian kernels that model the repulsive/attractive ranges for a cell positioned at x (i.e., at $s = 0$): $K_r(s) = \frac{1}{\sqrt{2\pi(s_r/8)^2}} \exp(-(x-s_r)^2/(2(s_r/8)^2))$, $K_a(s) = \frac{1}{\sqrt{2\pi(s_a/8)^2}} \exp(-(x-s_a)^2/(2(s_a/8)^2))$ with $s_r = 0.05$mm, $s_a = 0.3$mm. Shown here is $q_a K_a(s)$ and $q_r K_r(s)$, where the magnitudes of cell-cell repulsion and attraction are given by $q_r = 0.4$ and $q_a = 2$. **This type of Gaussian kernel incorporates the assumption that the repulsion force is stronger at some distance $s_r > 0$. This ensures that cells will not press on each other at almost zero spatial distances, causing them to pile up on top of each other (as it has been observed with Morse-type kernels, which have been considered more biologically realistic, but which can lead to density blow-up patterns [24]). Note that this kernel seems to describe the behaviour of cancer HeLa cells that have been shown to have a maximum diameter of $40\mu m$, which is then compressed to only $20\mu m$ when cells are in aggregations and press on each other [25, 26]. Finally, to give a more clear description of the interaction ranges (see also Appendix A), the inset figure in panel (b) shows the repulsive and attractive kernels on a logscale y-axis.**

now describes the tumour growth rate in the presence of TGF-β.
Note that the majority of models for tumour spread are of parabolic type, assuming a diffusion term that describes random cell movement. Here, we are interested mainly in the directed movement of cells (in response to each other, and as controlled by TGF-β) and thus we assume only advective movement. However, we emphasise that the turning rate λ_1 induces random cell movement, which in the parabolic limit leads to a diffusive term [28]. Since our focus is on directed cell movement (as described by the magnitude of λ_2), throughout this study we will assume that $\lambda_1 < \lambda_2$.

2. *The TGF-β molecules* diffuse at a constant rate D, and are produced at a rate p_e by the various cells in the environment (e.g., epithelial cells [29], monocytes and neutrophils [30] - considered here implicitly). Moreover, they are produced at a rate p_β by the tumour cells themselves [8]. Finally, the TGF-β molecules decay at a rate δ_β.

For the purpose of investigating the model analytically and numerically (see Sections 3 and 4), we assume a finite-length domain $[0, L]$ with periodic bound-

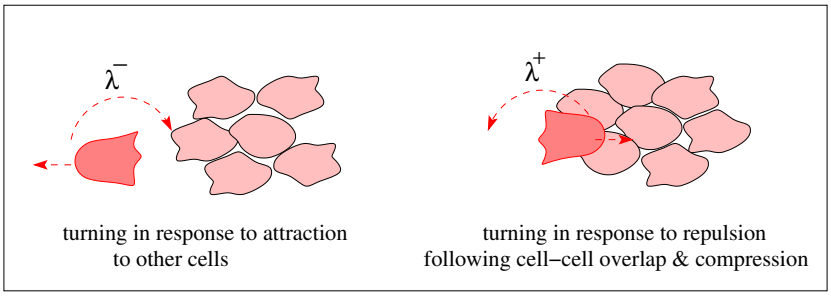

Figure 4: Caricature description of turning behaviour in cells, in response to attraction and repulsion signals from neighbouring cells.

ary conditions:

$$u_T^{\pm}(0,t) = u_T^{\pm}(L,t), \quad u_\beta(0,t) = u_\beta(L,t). \tag{5}$$

We note that these boundary conditions require the infinite integrals in (4) to be approximated by integrals over $[0, L]$, which are then wrapped around the domain. The kernels in these integrals (described in the caption of Fig. 3(b)) have an infinite support, but the parameters are chosen such that more than 99.99% of their mass is inside the interval $[0, L]$; see also the approach in [31].

3. Results: symmetry, steady states and their local stability

A first step in the investigation of model (1) focuses on studying its symmetry. This will enhance our understanding of the types of patterns exhibited by model (1).

3.1. Symmetry

We observe immediately that the solutions of model (1) are invariant under the translation symmetry:

$$\theta \cdot \mathbf{v}(x,t) = \mathbf{v}(x+\theta,t), \quad \theta \in [0,L), \tag{6}$$

where "$\cdot$" denotes the group action (see [32]), $\mathbf{v} = (u_T^+, u_T^-, u_\beta)$, and L is the length of the 1D domain. This invariance is due to the translation invariance of the differential and integral operators in (1) and the fact that the reaction terms are not space dependent. Because of the periodic boundary conditions, the translations can be interpreted as rotations and the group generated by the elements $\theta \in [0, L)$ can be identified with the rotation group $\mathbf{SO}(2)$. Moreover, the solutions of (1) satisfy the reflection symmetry:

$$\kappa \cdot (u_T^+(x,t), u_T^-(x,t), u_\beta(x,t)) = (u_T^-(L-x,t), u_T^+(L-x,t), u_\beta(L-x,t)). \tag{7}$$

Note that this symmetry sends the right-moving tumour cells at x into left-moving tumour cells at $L - x$, and vice-versa. Also, the symmetry moves the

TGF-β molecules from x to $L-x$. It is straightforward to verify that nonlocal interactions are preserved by these reflections:

$$\begin{aligned}
\kappa \cdot y_r^+(x) &= q_r \int_0^\infty K_r(s)\big(u_T(L-(x+s)) - u_T(L-(x-s))\big)ds \\
&= q_r \int_0^\infty K_r(s)\big(u_T((L-x)-s) - u_T((L-x)+s)\big)ds = y_r^-(L-x), \\
\kappa \cdot y_a^+(x) &= q_a \int_0^\infty K_a(s)\Big(\frac{u_T(L-(x+s))}{k_\beta + u_\beta(L-(x+s))} - \frac{u_T(L-(x-s))}{k_\beta + u_\beta(L-(x-s))}\Big)ds \\
&= q_r \int_0^\infty K_r(s)\Big(\frac{u_T((L-x)-s)}{k_\beta + u_\beta((L-x)-s)} - \frac{u_T((L-x)+s)}{k_\beta + u_\beta((L-x)+s)}\Big)ds \\
&= y_a^-(L-x).
\end{aligned}$$

Therefore, the turning rates satisfy

$$\kappa \cdot \lambda^\pm[u_T^+(x), u_T^-(x), u_\beta(x)] = \lambda^\mp[u_T^-(L-x), u_T^+(L-x), u_\beta(L-x)].$$

Because κ preserves the second order derivative with respect to space and does not affect the reaction terms, we can conclude that if $(u^+(x,t), u^-(x,t), u_\beta(x,t))$ is a solution of (1), then $\kappa \cdot (u^+(x,t), u^-(x,t), u_\beta(x,t))$ is also a solution. The group generated by the rotations θ and the reflection κ is identified with $\mathbf{O}(2)$, the group of symmetries of the circle. These results are summarised in the following statement:

Proposition 3.1. *Model (1) defined on the finite domain $[0, L]$ with periodic boundary conditions (5) is $\mathbf{O}(2)$ invariant, where the $\mathbf{O}(2)$ symmetry is given by (6)-(7).*

Overall, the existence of these symmetries in model (1), combined with the periodic boundary conditions (5), influences the type of solutions that could be exhibited by this nonlocal model. Moreover, the occurrence of stationary and moving aggregations of tumour cells (and TGF-β molecules) is also conditioned by the presence of steady-state and Hopf bifurcations - an aspect which will be investigated in the next two subsections in the context of spatially homogeneous states.

3.2. Spatially homogeneous steady states

To obtain a first understanding of the dynamics of model (1), we start investigating the spatially homogeneous steady-states, i.e., the states where all cells and the TGF-β molecules are equally spread over the whole domain ($\frac{\partial u_T^+}{\partial t} = \frac{\partial u_T^+}{\partial x} = 0$, $\frac{\partial u_T^-}{\partial t} = \frac{\partial u_T^-}{\partial x} = 0$, $\frac{\partial u_\beta}{\partial t} = \frac{\partial u_\beta}{\partial x} = 0$). Let us denote these steady-states by $(u_T^{+,*}, u_T^{-,*}, u_\beta^*)$, with the total cell density $u_T^* = u_T^{+,*} + u_T^{-,*}$.

Adding the right-hand-side terms in equations (1a) and (1b), leads to the following steady-state system for the total cell density u_T^* and TGF-β concentration u_β^* (note that the turning terms $\lambda^+ u_T^+$ and $\lambda^- u_T^-$ disappear when adding

(1a)+(1b)):

$$0 = p_T u_T^* \left(1 - \frac{u_T^*}{K_T}\right) - \delta_T u_T^* u_\beta^* (K_T^* - u_T^*), \tag{8a}$$

$$0 = p_e + p_\beta u_T^* - \delta_\beta u_\beta^*. \tag{8b}$$

The solutions of this system are:

- A tumour-free state: $(u_T^*, u_\beta^*) = (0, p_e/\delta_\beta)$. The TGF-$\beta$ molecules that persist in this case are produced by various cells in the environment (e.g., epithelial cells, monocytes, etc.). This state has $\mathbf{O}(2)$ symmetry.

- A tumour-present state: (u_T^*, u_β^*), which satisfies the following equations:

$$u_\beta^* = \frac{p_e + p_\beta u_T^*}{\delta_\beta}, \; u_T^* = \frac{-b \pm \sqrt{b^2 - 4ac}}{2a}, \tag{9}$$

with

$$a = \frac{\delta_T p_\beta}{\delta_\beta} > 0, \quad b = \frac{\delta_T (p_e - p_\beta K_T^*)}{\delta_\beta} - \frac{p_T}{K_T}, \quad c = p_T - \frac{\delta_T p_e K_T^*}{\delta_\beta}.$$

If $c < 0$, $b > 0$, or if $b^2 = 4ac$ and $b < 0$, there is one real and non-negative tumour-present state (u_T^*, u_β^*). However, if $0 < c < b^2/4a$ and $b < 0$, there are two real different tumour-present states. For the parameter values used for numerical simulations (see Section 4 and Table 2) we have $b < 0$, $c > 0$ such that $b^2 - 4ac > 0$, and model (1) has two tumour-present spatially homogeneous steady-states (see Fig. 5).

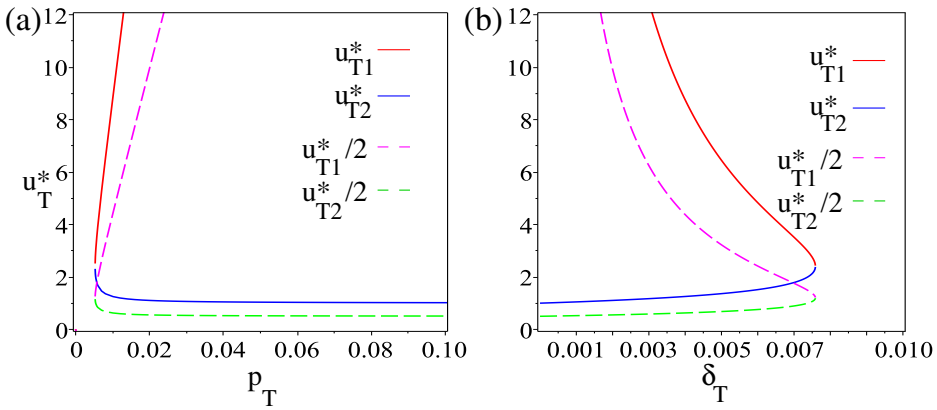

Figure 5: (a) Two tumour spatially-homogeneous steady states u_T^* given by equations (9), as we vary the tumour growth rate p_T; The states do not exist for very small p_T. (b) Two tumour spatially-homogeneous steady states u_T^* given by equations (9), as we vary the rate δ_T at which TGF-β influences tumour growth. The states do not exist for very large δ_T.

We note here that equations (8) are satisfied by the states with $u_T^{+,*} = u_T^{-,*} = u_T^*/2$. This result becomes clear if we observe that the terms $-\lambda^+ u_T^{+,*} + \lambda^- u_T^{-,*}$ in the steady-state equation corresponding to (1a) vanish because the integrals in (4) vanish, and thus the turning function in (3) reduces to a constant: $f = 0.5 - 0.5\tanh(m_0)$. If we denote by

$$\lambda^* = \lambda^{\pm}[u_T^{+,*}, u_T^* - u_T^{+,*}, u_\beta^*] = \lambda_1 + \lambda_2(0.5 - 0.5\tanh(m_0)),$$

we obtain $-\lambda^* u_T^* + \lambda^* u_T^* = 0$, which leads to equation (8a). For this reason, we graph in Figure 5 also the states $u_T^*/2$.

Next, we investigate the possibility of having tumour-present steady states with $u_T^{+,*} \neq u_T^{-,*} = u_T^* - u_T^{+,*}$ (i.e., states with $\mathbf{SO}(2)$ symmetry). Equating the steady-state expressions in (1a)-(1b) to eliminate the logistic terms (which are similar in these two equations), we obtain that the equilibria have to satisfy the following equation:

$$(u_T^{+,*} - u_T^{-,*})\Big(2\lambda^* + \delta_T u_\beta^*(K_T^* - u_T^*)\Big) = 0. \tag{10}$$

Therefore, we have two possibilities:

- $u_T^{+,*} = u_T^{-,*} = u_T^*/2$. As discussed before, in this case u_T^* satisfies equations (8), with the two explicit solutions given by (9); see also Figure 5). These states, where half of the tumour cells are facing right and half of the cells are facing left, have $\mathbf{O}(2)$ symmetry.
- $u_T^{+,*} \neq u_T^{-,*}$. From equation (10) we note that this state exists only when $2\lambda^* + \delta_T u_\beta^*(K_T^* - u_T^*) = 0$, which implies that we need $u_T^* > K_T^*$ and $2\lambda^* = \delta_T u_\beta^*(u_T^* - K_T^*)$. From this condition and the steady-state equation (1a) we obtain that

$$u_T^{+,*} = \frac{(\lambda^* + 0.5p_T(1 - u_T^*/K_t))u_T^*}{2\lambda^* + \delta_T u_\beta^*(K_T^* - u_T^*)} \quad \text{and} \quad u_T^{-,*} = u_T^* - u_T^{+,*}. \tag{11}$$

  However, a simple algebraic investigation of the conditions required for the existence of this state with $\mathbf{SO}(2)$ symmetry shows that for the parameter values chosen in this study (see Table 2), this steady state is unphysical.

3.3. Stability of spatially homogeneous steady states

To determine whether the dynamics of system (1) approach in the long-term the previously calculated spatially-homogeneous steady states, or some spatially-heterogeneous states, we perform a local stability analysis. First we consider the linearised version of system (1):

$$0 = \mathbf{u}_t + \mathcal{L}\mathbf{u} = \mathbf{u}_t + (\mathcal{L}_d + \mathcal{L}_l)\mathbf{u}, \tag{12}$$

where $\mathbf{u} = (u_T^+, u_T^-, u_\beta)^\top$, and the two linear operators are described by:

$$\mathcal{L}_d = \begin{pmatrix} \gamma\partial_x & 0 & 0 \\ 0 & -\gamma\partial_x & 0 \\ 0 & 0 & -D\partial_{xx} \end{pmatrix} \tag{13}$$

and

$$\mathcal{L}_l = \begin{pmatrix} -B_1^+ & -B_1^- & -B_1^\beta \\ -B_2^+ & -B_2^- & -B_2^\beta \\ -p_\beta & -p_\beta & \delta_\beta \end{pmatrix}, \tag{14}$$

where

$$\begin{aligned}
B_1^+ &= A_1 - \delta_T u_\beta^*(K_T^* - u_T^*) - u_T^*\lambda_2 f'(0) q_r (K_r^+ * - K_r^- *) \\
&\quad + u_T^*\lambda_2 f'(0) q_a (b_1 K_a^+ * + b_2 K_a^- *) - (\lambda_1 + \lambda_2 f(0)), && \text{(15a)} \\
B_1^- &= A_1 - u_T^*\lambda_2 f'(0) q_r (K_r^+ * - K_r^- *) + u_T^*\lambda_2 f'(0) q_a (b_1 K_a^+ * + b_2 K_a^- *) \\
&\quad + (\lambda_1 + \lambda_2 f(0)), && \text{(15b)} \\
B_2^+ &= A_2 + u_T^*\lambda_2 f'(0) q_r (K_r^+ * - K_r^- *) - u_T^*\lambda_2 f'(0) q_a (b_1 K_a^+ * + b_2 K_a^- *) \\
&\quad + (\lambda_1 + \lambda_2 f(0)), && \text{(15c)} \\
B_2^- &= A_2 - \delta_T u_\beta^*(K_T^* - u_T^*) + u_T^*\lambda_2 f'(0) q_r (K_r^+ * - K_r^- *) \\
&\quad - u_T^*\lambda_2 f'(0) q_a (b_1 K_a^+ * + b_2 K_a^- *) - (\lambda_1 + \lambda_2 f(0)), && \text{(15d)} \\
B_1^\beta &= -\delta_T u_T^{+,*}(K_T^* - u_T^*) + u_T^*\lambda_2 f'(0) q_a (b_3 K_a^+ * + b_4 K_a^- *), && \text{(15e)} \\
B_2^\beta &= -\delta_T u_T^{-,*}(K_T^* - u_T^*) - u_T^*\lambda_2 f'(0) q_a (b_3 K_a^+ * + b_4 K_a^- *). && \text{(15f)}
\end{aligned}$$

The terms A_1 and A_2 that appear in equations (15) are

$$\begin{aligned}
A_1 &= -\frac{p_T u_T^*}{2K_T} + \frac{p_T}{2}\Big(1 - \frac{u_T^*}{K_T}\Big) + \delta_T u_T^{+,*} u_\beta^*, \\
A_2 &= -\frac{p_T u_T^*}{2K_T} + \frac{p_T}{2}\Big(1 - \frac{u_T^*}{K_T}\Big) + \delta_T u_T^{-,*} u_\beta^*,
\end{aligned}$$

while the terms b_1, b_2, b_3 and b_4 that appear from the linearisation of the nonlocal attractive terms are

$$b_1 = \frac{1}{k_\beta + u_\beta^*} = -b_2, \quad b_3 = \frac{-u_T^*}{(k_\beta + u_\beta)^2} = -b_4. \tag{16}$$

Moreover, in equations (15) we defined the following convolutions

$$K_{r,a}^\pm * u = \int_0^\infty K_{r,a}(s) u(x \pm s) ds. \tag{17}$$

Next, we consider small perturbations of the spatially-homogeneous steady states, $u_T^\pm(x,t) = u_T^{\pm,*} + a_\pm \exp(ik_n x + \sigma t)$ and $u_\beta(x,t) = u_\beta^* + a_\beta \exp(ik_n x + \sigma t)$, where $k_n = 2\pi n/L$ is the wavenumber that emerges and σ describes the

growth of the perturbations. Substituting these terms into the linearised system $\mathbf{u}_t + \mathcal{L}\mathbf{u} = 0$, leads to the following Jacobian matrix:

$$J = \begin{pmatrix} \sigma + \gamma ik - B_1^+(k) & -B_1^-(k) & -B_1^\beta(k) \\ -B_2^+(k) & \sigma - \gamma ik - B_2^-(k) & -B_2^\beta(k) \\ -p_\beta & -p_\beta & \sigma + Dk^2 + \delta_\beta \end{pmatrix},$$

where the nonlocal terms $B_{1,2}^{\pm}(k)$ and $B_{1,2}^{\beta}(k)$ are defined in terms of the Fourier transforms of $K_{r,a}^{\pm}(k)$:

$$\hat{K}_{r,a}^+(k) = \int_0^\infty K_{r,a}(s)e^{iks}ds, \quad \hat{K}_{r,a}^-(k) = \int_0^\infty K_{r,a}(s)e^{-iks}ds. \tag{18}$$

The critical eigenvalues of this Jacobian are the solutions of the cubic equation

$$\sigma^3 + A\sigma^2 + B\sigma + C = 0, \tag{19}$$

where

$$\begin{aligned} A &= -B_2^- - B_1^+ + (Dk^2 + \delta_\beta), \\ B &= \gamma^2k^2 + \gamma ik(B_1^+ - B_2^-) + B_1^+B_2^- - B_1^-B_2^+ - p_\beta(B_1^\beta + B_2^\beta) \\ &\quad -(Dk^2 + \delta_\beta)(B_2^- + B_1^+), \\ C &= (Dk^2 + \delta_\beta)\big[\gamma^2k^2 + \gamma ik(B_1^+ - B_2^-) + B_1^+B_2^- - B_1^-B_2^+\big] \\ &\quad -p_\beta\big[B_2^+B_1^\beta + B_1^-B_2^\beta + \gamma ik(B_2^\beta - B_1^\beta) - B_1^\beta B_2^- - B_2^\beta B_1^+\big]. \end{aligned}$$

Note that for $u_T^{*,+} = u_T^{*,-} = 0$, the roots of the dispersion relation are:

$$\sigma_{1,2} = B_1^+ \pm \sqrt{(B_1^-)^2 - \gamma^2k^2}, \qquad \sigma_3 = -Dk^2 - \delta_\beta < 0. \tag{20}$$

Thus we can summarise the stability of this tumour-free state in the following result (see also Figure 6(a)):

Proposition 3.2. *The tumour-free steady state $(u_T^{*,+}, u_T^{*,-}, u_\beta) = (0, 0, p_e/\delta_\beta)$ is unstable provided that $(B_1^-)^2 - (B_1^+)^2 \geq \gamma^2k^2$. The first wavenumbers that become unstable have low modes, and the patterns arise via steady-state bifurcation. Moreover, the stability of this steady state does not depend on the magnitudes of cell-cell adhesion and repulsion (q_a and q_r).*

In regard to the $\mathbf{O}(2)$ tumour-present steady states we can show below a stability result for $q_a = q_r = 0$. While this case makes the model trivial, the result will allow us to confirm analytically, when we will graph the neutral-stability curves in the $q_a - q_r$ plane (see Figure 8), that the open region having the origin (q_aq_r)=(0,0) at its boundary corresponds to asymptotic stability of the tumour-free steady-state. The case $q_{r,a} > 0$ is not investigated analytically, but rather graphically by determining the neutral stability curves, see Section 3.3.1):

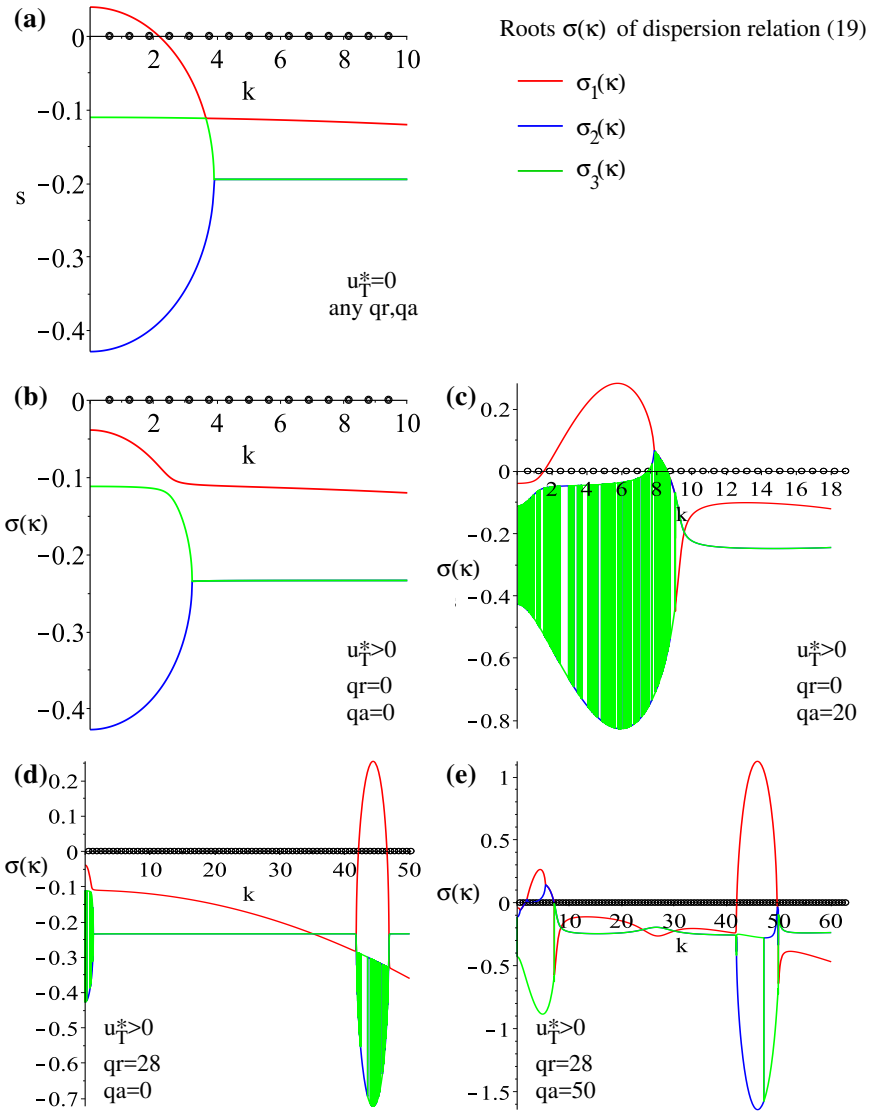

Figure 6: Dispersion relation (σ vs. k) for the steady states with $\mathbf{O}(2)$ symmetry $(u_T^{*,+}, u_T^{*,-}, u_\beta^*)$, where $u_T^{*,+} = u_T^{*,-}$. (a) Tumour-free state ($u_T^{*,\pm} = 0$); Its stability does not depend on q_a or q_r. (b)-(e) Tumour-present steady state (state u_{T2}^* from Figure 5); Its stability depends on q_a and q_r. For low q_r, q_a the state is stable (panel (b)). Increasing q_a leads to instability to low wavenumbers (k_6 – shown in the inset figure in panel (c)). Increasing q_r leads to instability to high wavenumbers (k_{71} – shown in the inset figure in panel (d)). Increasing both q_r and q_a leads to instability to both low and high wavenumbers (panel (e)). Here $p_T = 0.04$, and the rest of parameters are as in Table 2. The points on the x-axis represent the discrete wavenumbers $k_j = 2\pi j/L$.

Proposition 3.3. *The tumour-present steady state* $(u_T^*/2, u_T^*/2, u_\beta)$ *is asymptotically stable for* $q_a = q_r = 0$ *provided that the model parameters are such that the following conditions hold:*

$$p_T > \delta_T u_T^* u_\beta^*, \tag{21a}$$

$$u_T^* > K_T, \tag{21b}$$

$$2\big(\lambda_1 + \lambda_2 f(0)\big) > p_T\Big(\frac{u_T^*}{K_T} - 1\Big), \tag{21c}$$

$$\delta_\beta\big(\frac{p_T}{K_T} - \delta_T u_\beta^*\big) > (u_T^* - K_T^*)p_\beta\delta_T. \tag{21d}$$

This result is proved in Appendix C. For the parameter values described in Table 2, all these three conditions hold true (see also Figure 6(b)). Note that we can interpret conditions (21) from a biological perspective. For example, condition (21a) states that tumour proliferation rate must be much higher than the rate of tumour inhibition/growth as determined by the TGF-β molecules. Condition (21b) states that the tumour must grow (slightly) above the carrying capacity (as a result of the pro-tumour effect of the TGF-β cytokines). Condition (21c) states that the (random/directed) turning rates of the tumour cells must be relatively large (to overcome the rate of tumour growth). Finally, condition (21d) states that the decay rate δ_β of the TGF-β molecules must be high enough (to counterbalance the production rate of TGF-β and the rate of tumour inhibition/growth in the presence of TGF-β). This last condition suggests that a low decay rate δ_β (associated with a persistence of high TGF-β levels) leads to instability of the tumour-present steady state $(u_T^*/2, u_T^*/2, u_\beta)$ and thus induces the formation of tumour aggregations.

In Figure 6 we graph the three solutions σ_j, $j = 1, 2, 3$ of equation (19) as a function of the wavenumber k, for the tumour-present steady-states $(u_T^{*,+}, u_T^{*,-}, u_\beta^*)$ with $\mathbf{O}(2)$ symmetry (i.e., $u_T^{*,+} = u_T^{*,-}$). Here, $p_T = 0.04$ and the rest of parameter values are as described in Table 2. Panel (a) shows the stability of the state with $u_T^{*,+} = u_T^{*,-} = 0$, while panels (b)-(e) show the stability of a state with $u_T^{*,+} = u_T^{*,-} > 0$. We remark that increasing q_a leads to instability to low wavenumbers (panel (c)), while increasing q_r leads to instability to high wavenumbers (panel (d)). In terms of pattern formation, low wavenumbers correspond to a small number of large cell aggregations, while high wavenumbers correspond to a large number of small cell aggregations (i.e., a sort of metastasis phenomena).

To gain a better understanding of the previous stability results, in Figure 7 we show the neutral stability curves $\sigma(k) = 0$ for different (discrete) wavenumbers k_j (i.e., $j \in [1, 16]$ in panel (a); $j \in [1, 80]$ in panel (b)). Panel (a) confirms that, for the steady states $u_T^* = 0$, the neutral stability curves do not depend on q_a or q_r, and the first three wavenumbers (k_j, $j = 1, 2, 3$) are always unstable (for the parameter values in Table 2). Panel (b) shows that, for the steady states $u_T^* > 0$, when we keep q_a fixed and vary q_r, then small q_r is associated

with instability of low wavenumbers (i.e., $k_j < 10$) while large q_r is associated with instability of high wavenumbers (i.e., $k_j > 30$). When we fix q_r and vary q_a, then instability of low wavenumbers appears only for large q_a. Note the for $q_a > 50$ one could also observe instability of high wavenumbers (i.e., $k_j > 30$; corresponding to the case in Figure 6(e)) - not shown here.

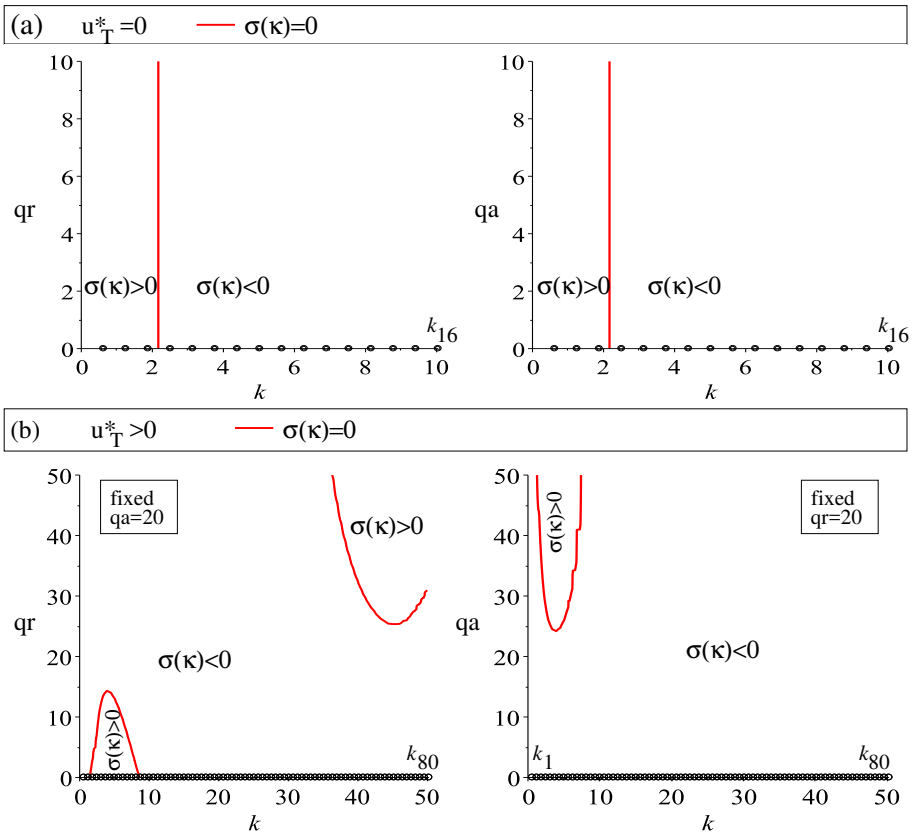

Figure 7: Neutral stability curves ($\sigma(k) = 0$) for (a) tumour-free state $u_T^* = 0$, (b) tumour-present state u_T^* (with $u_T^{+,*} = u_T^{-,*}$). Left panels show the neutral stability curves in the (q_r, k) space, while right panels show the neutral stability curves in the (q_a, k) space. The points on the x-axis represent the discrete wavenumbers $k_j = 2\pi j/L$. For the left panel in (b) we fix $q_a = 20$ and we vary q_r. For the right panel in (b) we fix $q_r = 20$ and we vary q_r.

Since for the parameters values in Table 2 the tumour-free and tumour-present steady-states are all unstable, the final transient pattern will likely be influenced by the most unstable wavenumbers in all states. In this case we expect that the patterns will be influenced by various mode-mode interactions.

In the following, we confirm our results on the role of q_r and q_r on the dispersion relation $\sigma(k)$ using a second method, which leads to the creation of bifurcation diagrams showing neutral stability curves for different wavenumbers.

267 *3.3.1. Neutral stability curves*

The following derivation is similar to the one found in [33] and we omit most of the calculations. We consider the action of the group $\mathbf{O}(2)$ described in (6), on functions in the space

$$X = \{u = (u^+, u^-, u^\beta) \in W^{1,p}([0, L], \mathbb{R}^3) \mid u(0) = u(L)\}.$$

Then,

$$X_n = \{ae^{ik_n x} + c.c \mid a = (a^+, a^-, a^\beta) \in \mathbb{C}^3\}$$

is a $\mathbf{O}(2)$-invariant subspace of X and it is straightforward to verify that X is a direct sum of the X_n spaces. Let

$$f_1 = (1, 1, 0)^T, \quad f_2 = (1, -1, 0)^T, \quad f_3 = (0, 0, 1).$$

Then, each subspace

$$X_n^j = \{(v_j e^{ik_n x} + \overline{v}_j e^{-ik_n s}) f_j \mid v_j \in \mathbb{C}\}$$

is $\mathbf{O}(2)$ irreducible and they are $\mathbf{O}(2)$ isomorphic. It is straightforward to verify that $X_n = X_n^1 \oplus X_n^2 \oplus X_n^3$. Therefore, the $\mathbf{O}(2)$ invariant subspaces form an isotypic decomposition of X and in particular, $\mathcal{L}(X_n) \subset X_n$. Thus, the linearization $\mathcal{L}$ block decomposes into 3×3 matrices $\mathcal{L}_n$ and we write these matrices in the basis given by the three vectors $v_j e^{ik_n x} f_j$, $j = 1, 2, 3$ and $v_j \in \mathbb{C}$. We obtain $\mathcal{L}_n$ by applying $\mathcal{L}_d$ and $\mathcal{L}_\ell$ on those vectors. We set

$$M_1 = A_1 - \delta_T u_\beta^*(K_T^* - u_T^*) - \lambda^* \quad \text{and} \quad M_2 = A_2 + \lambda^*.$$

Note that we write

$$2i\widetilde{K}_r(k_n) = \hat{K}_r^+(k_n) - \hat{K}_r^-(k_n) \quad \text{and} \quad 2i\widetilde{K}_a(k_n) = (\hat{K}_a^+(k_n) - \hat{K}_a^-(k_n)).$$

because the right hand sides of the above equalities are purely imaginary and so $\widetilde{K}_{r,a}$ are real. Finally, we write

$$P^+ = \delta_T u_T^{+,*}(K_T^* - u_T^*) \quad \text{and} \quad P^- = \delta_T u_T^{-,*}(K_T^* - u_T^*).$$

Note that at a $\mathbf{O}(2)$-symmetric equilibrium, $A_1 = A_2$ and $P := P^+ = P^-$. Let $\phi_n(x) = (v_1, v_2, v_3)e^{ik_n x}$. A straightforward computation and simplifications lead to $\mathcal{L}_n\phi_n(x) =$

$$\begin{pmatrix} -(M_1 + M_2) & i\gamma k_n & -P \\ 4iu_T^*\lambda_2 f'(0)(q_r\widetilde{K}_r - q_a b_1 \widetilde{K}_a) + i\gamma k_n & -(M_1 - M_2) & -2iu_T^*\lambda_2 f'(0) q_a b_3 \widetilde{K}_a \\ -2p_\beta & 0 & \delta_\beta \end{pmatrix} \phi_n(x).$$

We determine the formula for the neutral stability curves corresponding to zero eigenvalues by computing the determinant of $\mathcal{L}_n$. We obtain $\det(\mathcal{L}_n) =$

$$\begin{aligned} \delta_\beta((M_1^2 - M_2^2) + \gamma^2 k_n^2 + 4\gamma k_n u_T^* \lambda_2 f'(0)(q_r\widetilde{K}_r(k_n) - q_a b_1 \widetilde{K}_a(k_n))) \\ -2p_\beta(2\gamma k_n u_T^* \lambda_2 f'(0) q_a b_3 \widetilde{K}_a(k_n) - P(M_1 - M_2)) \end{aligned}$$

which is a linear function of q_r and q_a. We solve $\det(\mathcal{L}_n) = 0$ as

$$q_r = \frac{-\delta_\beta((M_1^2 - M_2^2) + \gamma^2 k_n^2) - 2p_\beta P(M_1 - M_2)}{4\gamma k_n u_T^* \lambda_2 f'(0)\widetilde{K}_r(k_n)} + \frac{(\delta_\beta b_1 + 4p_\beta b_3)\widetilde{K}_a(k_n)}{\widetilde{K}_r(k_n)} q_a. \tag{22}$$

We explore equation (22) for parameter values in Table 2. The numerator of the constant term is negative for $n \geq 2$ and $\widetilde{K}_r(k_n) > 0$ for $n = 1, \ldots, 50$ and negative for $n = 51, \ldots, 100$. The slope of the line depends on the ratio $\widetilde{K}_a(k_n)/\widetilde{K}_r(k_n)$ and a graph is shown in Figure 8(a). A subset of the neutral stability lines are graphed in Figure 8(b).

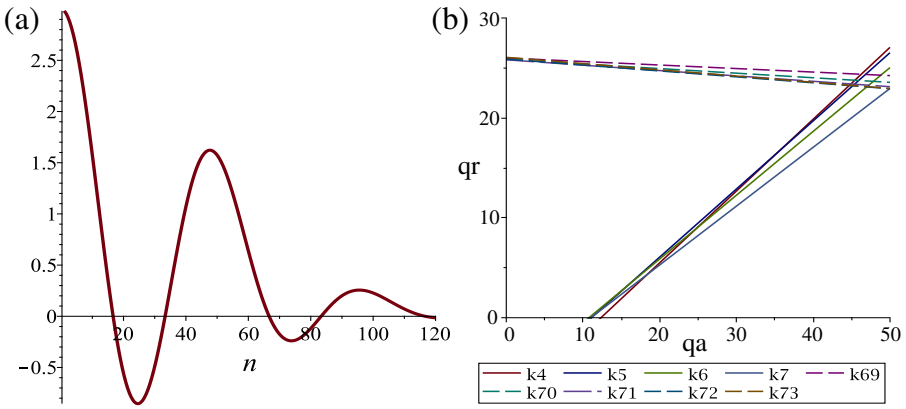

Figure 8: (a) Ratio $\widetilde{K}_a(k_n)/\widetilde{K}_r(k_n)$ as a function of n. (b) Examples of neutral stability lines determining the boundary of the asymptotic stability region of the nonzero $\mathbf{O}(2)$ equilibrium. Dashed lines show the neutral stability lines corresponding to high wavenumbers (e.g., here we graph $k_{69} - k_{73}$), while continuous lines show the neutral stability lines corresponding to low wavenumbers (e.g., here we graph $k_4 - k_7$).

For the parameter values satisfying Theorem 3.3, the region in Figure 8(b) that contains $(0, 0)$ and is bounded by the neutral stability lines, encloses the asymptotic stability region for the $\mathbf{O}(2)$ symmetric equilibrium. Thus, we see that the neutral stability lines with positive slope bounding the region of asymptotic stability have low wave numbers $(k_4, \ldots, k_7)$ while the neutral stability lines with negative slope bounding the region of asymptotic stability have high wave numbers $(k_{69}, \ldots, k_{74})$.

We conclude by mentioning that Hopf bifurcations do not occur for the parameter values chosen in this paper. This can be observed by computing $\det(\mathcal{L}_n - \sigma i I) = 0$ which leads to a characteristic equation of the form $i\sigma^3 + c_2\sigma^2 + ic_1\sigma + c_0 = 0$ leading to two equations $\sigma^2 + c_1 = 0 = c_2\sigma^2 + c_0$ and therefore a line of purely imaginary eigenvalues exists given that $c_0 - c_1 c_2 = 0$. In our case, this equation leads to a line entirely in the third quadrant of the (q_a, q_r) plane. The details can be verified by the interested reader.

In the following section, we investigate numerically the patterns displayed by model (1), when we perturb randomly (i) spatially homogeneous steady states

$(u_T^{+,*}, u_T^{-,*}, u_\beta^*)$, and (ii) an initial small aggregation of cells described by a step function.

4. Numerical results

For the numerical simulations, we discretise model (1) on a 1D dimensional domain of length $L = 10$ mm, and assume periodic boundary conditions given by equation (5). The numerical integration is based on a time splitting method, which calculates first the time propagation of the diffusion and advection parts, and then the time-propagation of the reaction part. Equations are first discretised in space on a uniform mesh with space step $\Delta x = 10^{-2}$ mm, and the system is then discretised in time with a time step $\Delta t = \frac{1}{3}10^{-2}$ day (chosen to satisfy the Courant-Friedrichs-Lewy condition for the stability of the upwind/downwind numerical schemes). The diffusion term is discretised using the Crank-Nicholson method (with periodic boundary conditions), while the advective term is discretised using the upwind/downwind scheme (also with periodic boundary conditions). For the reaction term we use the 4th order Runge-Kutta method. The nonlocal attraction-repulsion terms are approximated using Simpson's method (with periodic boundary conditions that see the nonlocal terms being wrapped around the domain). The numerical codes were written in C.

In the following two subsections we show the result of numerical simulations when we vary two parameters: the cell-cell adhesion factor q_a, and the proliferation rate p_T. In Section 4.1 we vary $q_a \in [20, 80]$, when the tumour proliferation rate is $p_T = 0.04$ (as observed in B16 melanoma murine tumours, which have a doubling time between 14-24 hours, corresponding to tumour proliferation rates between 0.028-0.049). Since for $q_a \leq q_r = 10$ we do not observe any spatio-temporal patterns (i.e., the solutions approach the stable spatially homogeneous steady states – see also Figures 7(b) and 8), we present only the results of the simulations obtained with $q_a \gg q_r$. To investigate (from a theoretical point of view) what happens if we increase the proliferation rate of tumour cells, in Section 4.2 we discuss the case $p_T = 0.4$. All other parameter values are fixed, as described in Table 2.

Finally, for the numerical simulations we use two types of initial conditions:

- random perturbations of nonzero spatially homogeneous steady states $(u^{+,*}, u^{-,*}, u_\beta^*)$, to describe the formation of tumour aggregations when tumour cells are equally spread over the whole domain:

$$u_T^{\pm}(x) = u_T^{\pm,*} + rand(0, 0.01), \quad u_\beta^{\pm}(x) = u_\beta^* + rand(0, 0.01). \tag{23}$$

- step function, to describe an already formed small tumour:

$$u_T^{\pm}(x) = u^*, \text{ for } x \in \left[\frac{3}{10}, \frac{4}{10}\right], \text{ and } u_T^{\pm}(x) = 0 \text{ elsewhere}, \tag{24a}$$

$$u_\beta(x) = u_b^*, \text{ for } x \in \left[\frac{3}{10}, \frac{4}{10}\right], \text{ and } u_T^{\pm}(x) = \epsilon \text{ elsewhere}, \tag{24b}$$

with $u_b^* \gg \epsilon > 0$ to describe the higher level of TGF-β molecules at the position of the tumour. Note that it is possible to have low levels of TGF-β also outside the tumour since these cytokines can be produced by other types of cells: normal epithelial cells, immune cells, etc. For $p_T = 0.4$ we choose $\epsilon = 0.1$, while for $p_T = 0.04$ we choose $\epsilon = 0.01$.

4.1. Lower tumour proliferation rates

To investigate the dynamics of weakly-aggressive tumour cell lines, we perform numerical simulations with proliferation rate $p_T = 0.04$. We vary the magnitude of the cell-cell attraction force for two types of initial conditions: random perturbations of the spatially homogeneous steady states given by equations (9)-(11) (see Figure 9), and step-function initial conditions to describe an initial tumour aggregation of maximum size $u^* = 0.036$ (see Figure 10).

Figure 9 shows the dynamics of model (1) for small (panels (a)-(d)), medium (panels (a')-(d')) and large (panels (a")-(d")) attractive interactions between cells. For small and intermediate attraction, the transient dynamics of the model (i.e., dynamics for $t \in (200, 650)$) is characterised by the formation of new aggregations of cells at distant positions in space, followed by the movement of these aggregations. These new aggregations form due to continuous cell proliferation, combined with the appearance of new space between existing aggregations. In some cases, these aggregations collide with other aggregations moving in opposite directions (due to cell-cell attraction). The asymptotic dynamics of the model is characterised by classical solutions: rotating waves (i.e., moving aggregations of cells) and stationary pulses (i.e., stationary aggregations of cells). In fact, the rotating waves exist for small cell-cell attractive interactions, while the stationary pulses exist for large cell-cell attractive interactions. Note that the bias to the left of the rotating waves is likely a random choice of direction, due to the appearance of new cell aggregations at positions in space between already formed cell aggregations, and the nonlocal interactions between these cells.

The transient phenomenon characterised by the formation of new cell aggregations (formed of newly-proliferating cells and cells that broke off from existent aggregations) can be seen more clearly in Figure 10, where we start the numerical simulations assuming an already-formed tumour. Again, for low cell-cell attractive interactions ($q_a = 20$) these newly-formed cellular aggregations move around the domain (due to periodic boundary conditions), while for high attractive interactions ($q_a = 40, 80$) the aggregations are stationary. We note here that the different initial conditions in Figures 9-10 do not seem to impact the asymptotic dynamics of model (1).

Remark 4.1. *We emphasise that the transient behaviour of arising and merging cell aggregations is the result of cell growth, in the context of a dominating wavelength. It is likely that this behaviour is the results of unstable spatial heterogeneous patterns (see the discussion in [34]). However, due to the nonlocal terms in model (1), an analytical investigation of the stability of these heterogeneous states is very difficult, and beyond the scope of this paper. The asymptotic*

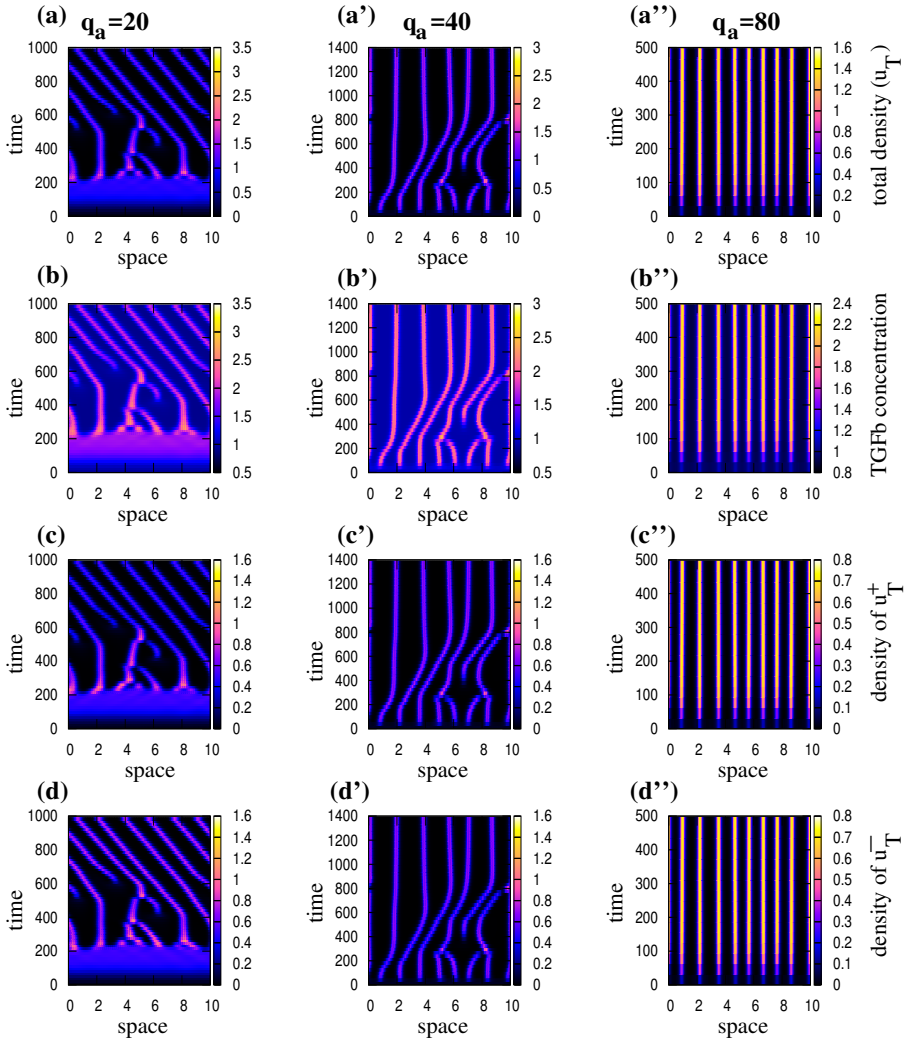

Figure 9: Dynamics of model (1) for $p_T = 0.04$ and for initial conditions given by equations (23). Panels (a)-(d): model dynamics when $q_a = 20$; Panels (a')-(d'): model dynamics when $q_a = 40$; Panels (a")-(d"): model dynamics when $q_a = 80$. The rest of parameter values are as in Table 2. Finally, panels (a)-(a") show total tumour density, panels (b)-(b") show TGF-β concentration, panels (c)-(c") show u_T^+, and panels (d)-(d") show u_T^-.

behaviour of the system is described by classical patterns: stationary pulses and rotating waves, which are prevalent in differential equations with $\mathbf{O}(2)$ *symmetry.*

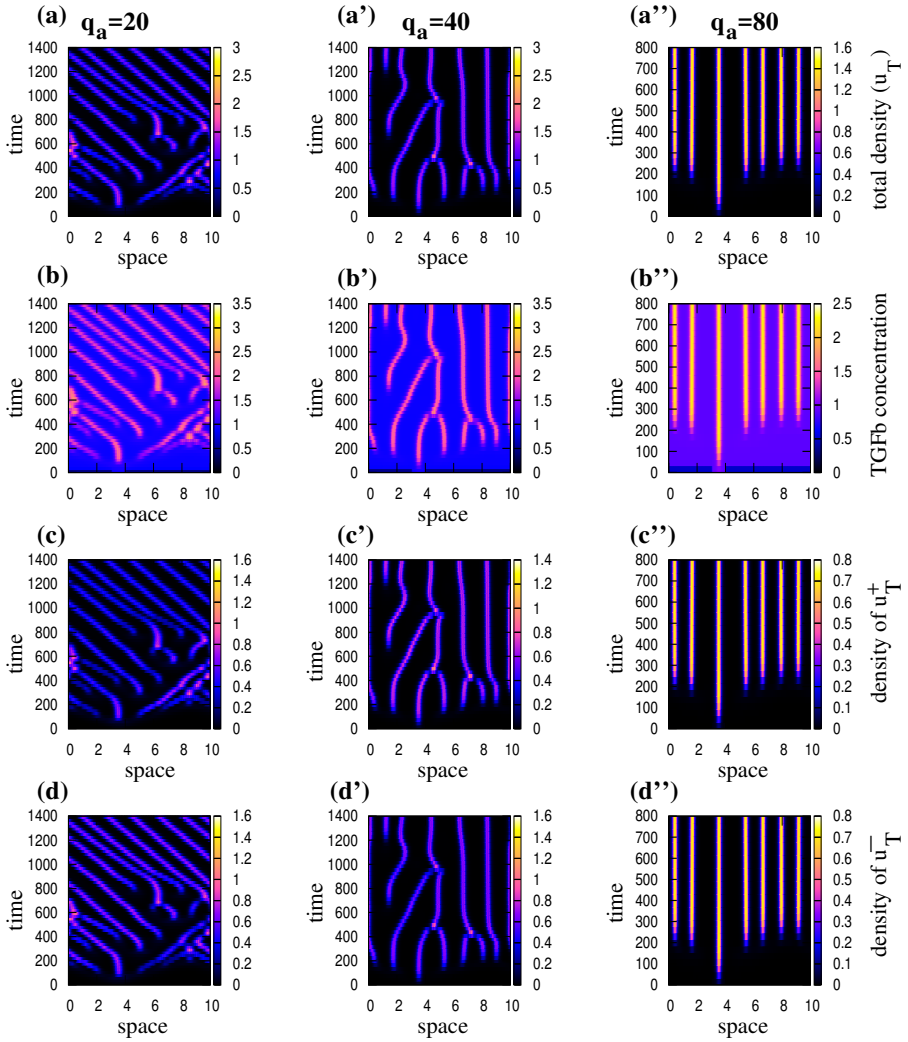

Figure 10: Dynamics of model (1) for $p_T = 0.04$ and for initial conditions given by equations (24). Panels (a)-(d): dynamics when $q_a = 20$; Panels (a')-(d'): dynamics when $q_a = 40$; Panels (a")-(d"): dynamics when $q_a = 80$. The rest of parameter values are as in Table 2. Finally, panels (a)-(a") show total tumour density, panels (b)-(b") show TGF-β concentration, panels (c)-(c") show u_T^+, and panels (d)-(d") show u_T^-.

4.2. High tumour proliferation rate

In Figure 11 we investigate the dynamics of model (1) when we increase p_T to $p_T = 0.4$. We see that in this case, low cell-cell adhesive interactions lead to a spread of cells over the whole domain (see panels (a),(b) and (c),(d)). Higher cell-cell adhesion leads to the formation of moving aggregations (which persist even for very high cell-cell adhesion - e.g., $q_a = 120$; not shown here). For initial

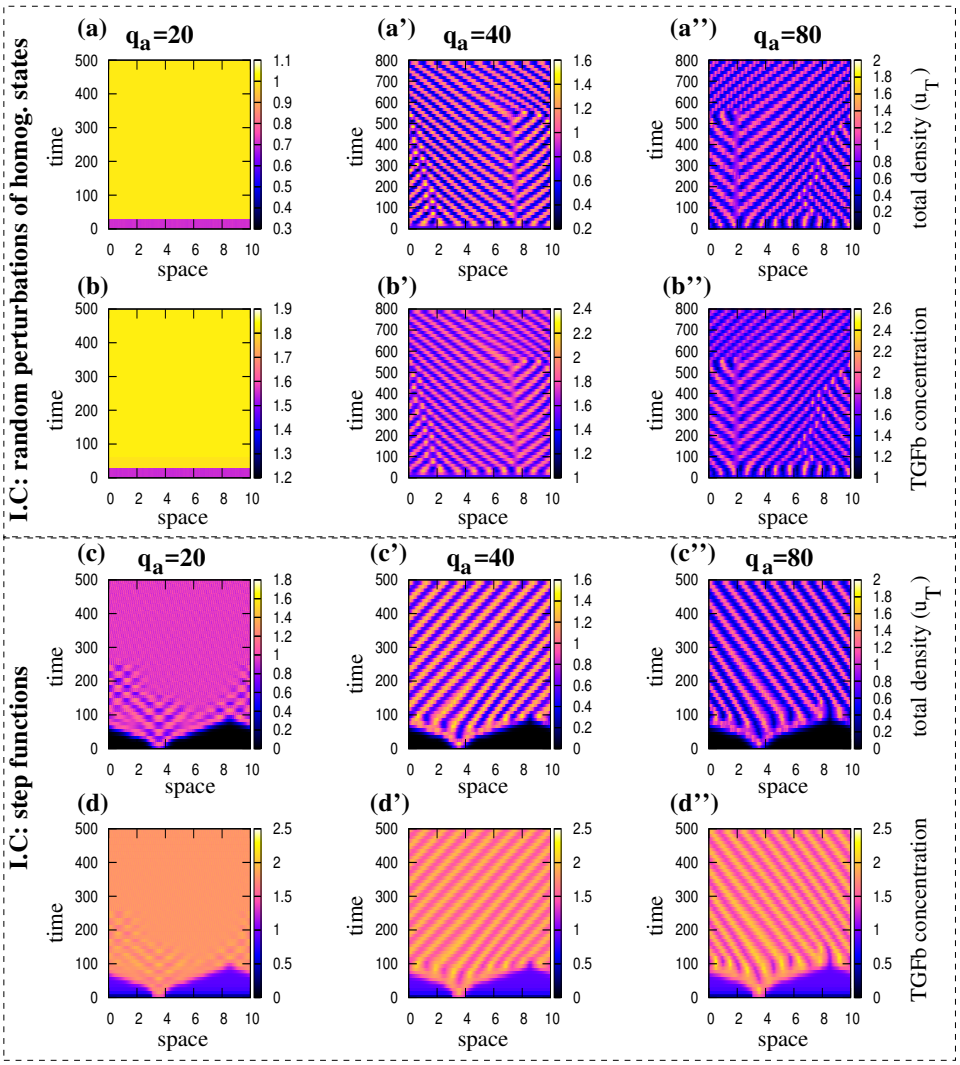

Figure 11: Dynamics of model (1) for $p_T = 0.4$ and for initial conditions given by equations (23) - panels (a)-(b"), and equations (24) - panels (c)-(d"). We show only the total tumour density u_T (panels (a)-(a") and (c)-(c")) and the concentration of TGF-β molecules (panels (b)-(b") and (d)-(d")).

conditions that are random perturbations of the homogeneous steady states (see top panels (a'),(b') and (a"),(b")), the transient dynamics shows small groups of tumour cells that break off from existent moving aggregations, and choose to move either left or right (giving rise to a topological defect line that persists up to $t \approx 600$). Then, because of the periodic boundary conditions, these new aggregations collide with other aggregations that move in the opposite direction.

This type of transient dynamics is not observed for initial conditions described by step functions with $u^* = 0.39$ and $u_b^* = 1.3$ – panels (c)-(d") (at least not for the parameter space investigated in this study). Again, we note that the different initial conditions in Figure 11 (top and lower panels) do not seem to impact the asymptotic dynamics of model (1).

4.3. Sensitivity to TGF-β

Since TGF-β plays an important role on tumour dynamics, next we perform a local sensitivity analysis to investigate the effect of small changes in δ_T, p_β, and k_β (we ignore δ_β since we assume that the degradation rate of this cytokine is more or less fixed). To this end, we vary these three parameters by $\pm$ 80% (see Table 1). Fourth column in Table 1 shows the range in the percentage change in tumour size, corresponding to changes in parameter values (for both homogeneous and step-like initial conditions). For simplicity, we focus only on the case $p_T = 0.04$.

Param.	Baseline	Param. range (baseline$\pm$80%)	% Change in total tumour size u_T on day 140 (compared to baseline)
δ_T	0.001	$(0.0002, 0.0018)$	Homog. IC: $(-0.03\%, 0.033\%)$
			Step-like IC: $(-0.0189\%, 0.02\%)$
p_β	0.1	$(0.02, 0.18)$	Homog. IC: $(-0.5948\%, 0.0146\%)$
			Step-like IC: $(-0.09\%, 0.19\%)$
k_β	0.1	$(0.02, 0.18)$	Homog. IC: $(-0.149\%, 0.0001\%)$
			Step-like IC: $(-0.0449\%, 0.048\%)$

Table 1: Sensitivity of tumour cells to changes in TGF-β parameters. We investigate the percentage change in total tumour density on day $t = 140$, $U_T(140) = (1/L)\int_0^L (u_T^+(x, 140) + u_T^-(x, 140))dx$, using the formula: $[U_T^{new}(140) - U_T^{baseline}(140)]/[U_T^{baseline}(140)]$ (for both homogeneous and step-like initial conditions). Here we assume $p_T = 0.04$, $q_a = 20$, $q_r = 10$, and all other parameters as in Table 2.

Figure 12 shows the change in the total tumour cell density on day $t = 140$ ($U_T(140) = \int_0^T (u_T^+(x, 140) + u_T^-(x, 140))dx$), as the three parameters associated with TGF-β are varied by $\pm$80% (for both homogeneous and step-like initial conditions). Note that an increase in parameters values leads to an increase in tumour size, while a decrease in parameter value leads to a decrease in tumour size (irrespective of the initial conditions). We also note the different magnitudes of changes in tumour growth (on day $t = 140$) for different initial conditions. Finally, we emphasise that the parameter that induces the largest variations in tumour size on day $t = 140$ is p_β – the production of TGF-β molecules by the tumour cells.

Figure 13 shows the effect of parameter changes on the growth of tumour cells until day 140 (panels (a)-(c)), and on the spatial structure of the tumour on day 140 (panels (a')-(c')), for homogeneous initial conditions. We observe that an increase in the parameter values leads not only to larger tumours on day 140 (as shown in Figure 12), but also to a delay in the formation of spatial aggregations

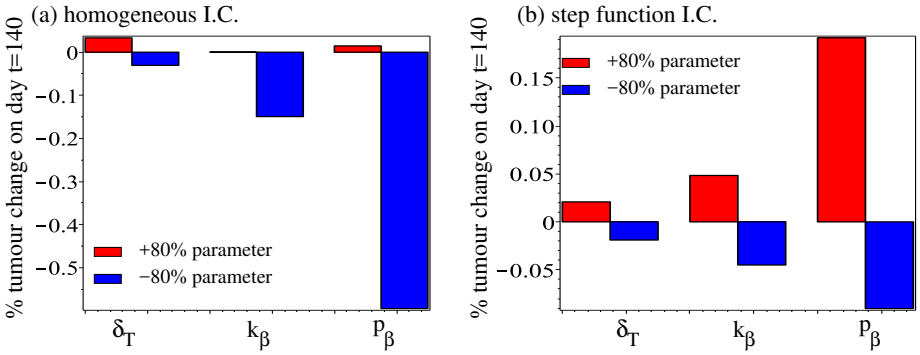

Figure 12: Changes in total tumour size at time $t = 140$, as the three parameters associated with TGF-β, δ_T, k_β, p_β, are changed by $\pm 80\%$. (a) Initial conditions for simulations are perturbations of homogeneous steady states; (b) Initial conditions for simulations are step-like functions.

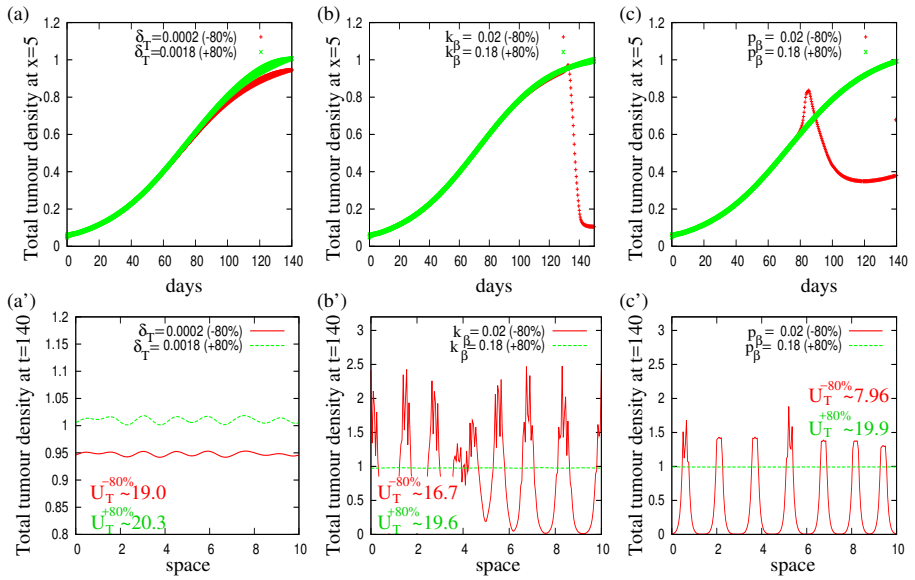

Figure 13: Tumour density ($u_T^+ + u_T^-$) as we vary three parameters associated with TGF-β (δ_T, k_β, p_β) by $\pm 80\%$ (see values in Table 1). Panels (a), (b), (c) show the time-growth of tumour cells at spatial position $x = 5$. Panels (a'),(b'),(c') show the spatial distribution of tumour cells at time $t = 140$ days. Here we consider $q_a = 20$, $q_r = 10$, $p_T = 0.04$ and all other parameters are as in Tables 1 and 2. Total tumour density corresponding to the parameter values changed by $\pm 80\%$, as calculated using formula $U_T(140) = (1/L)\int_0^L (u_T^+(x,140) + u_T^-(x,140))dx$, is as follows: (a') $U_T(140)^{-80\%} = 19.05$, $U_T(140)^{+80\%} = 20.308$; (b') $U_T(140)^{-80\%} = 16.718$, $U_T(140)^{+80\%} = 19.65$; (c') $U_T(140)^{-80\%} = 7.96$, $U_T(140)^{+80\%} = 19.94$.

of cells. Since the formation of these cellular aggregations can be associated with a synchronous metastasis-like process (where cells form new aggregations

at distant positions in space), this result suggests an interesting behaviour in tumour dynamics: smaller tumours could lead to faster synchronous metastasis. While many clinical studies focused on the correlation between the size of the tumour and the probability for synchronous metastases [35, 36, 37, 37, 38, 39, 40], these results are sometimes contradictory. For example, there are a few studies on renal tumours which could not find any correlations between the size of (relatively small) tumours and their metastatic potential [37]. However, many other studies supported such a correlation, with larger tumours having a higher probability for synchronous metastasis in renal or breast tumours [35, 36, 37, 39].

It should be emphasised that all these clinical studies look at the size of the primary tumour following detection and treatment. In Figure 14(a)-(c) we consider step-like initial conditions, and show the spatial distribution of tumour cells on day $t = 140$, as we vary three parameters associated with TGF-β: δ_T, k_β and p_β. We note that for δ_T and k_β there are no significant differences in the spatial distribution of tumour cells at this initial time (t=140 days). Only an increase in p_β (associated with an increased total tumour size) leads to a faster spatial spread of secondary tumour aggregations further away from the primary aggregation; see Figure 14(c). This behaviour could be associated with an increased metastatic potential, thus suggesting that larger tumours could spread faster. In Figure 14(a')-(c') we show the spatial distribution of tumour cells at a later time, $t = 800$ (with the inset showing a space-time plot for the case where parameters are increased by 80%). Again, there are no significant differences between the patterns obtained when we vary δ_T and k_β. However, increasing p_β leads to tumour invasion of larger territories.

Remark 4.2. ***The results in this section were obtained for*** $s_r = 0.1$ ***(see Table 2). This repulsion range required strong attractive cell-cell interactions for aggregation patterns to form. However, we investigated pattern formation also with smaller repulsive ranges:*** $s_r = 0.01$ ***(not shown here). In this case, we obtained patterns similar to those in Figures 9, 10, but for much smaller attractive cell-cell interactions:*** $q_a = 15$, $q_a = 20$ ***and*** $q_a = 30$. ***Hence, the size of the repulsion range (which can be related to the strength of the compressive stress) influences the strength of cell-cell adhesion that leads to the formation and movement of small cancer cell aggregations. Note that experimental results have shown that increased cell-cell compressive stress (as a result of tumour growth) leads to increased motility of aggressive tumour cells and cancer cell invasion [41].***

5. Summary and Discussion

In this study we derived a new 1D mathematical model for the dynamics of tumour cells in response to TGF-β molecules produced by themselves and by other cells in the tumour microenvironment. (A 2D version of this model is presented in Appendix B.) We then used this mathematical model to investigate

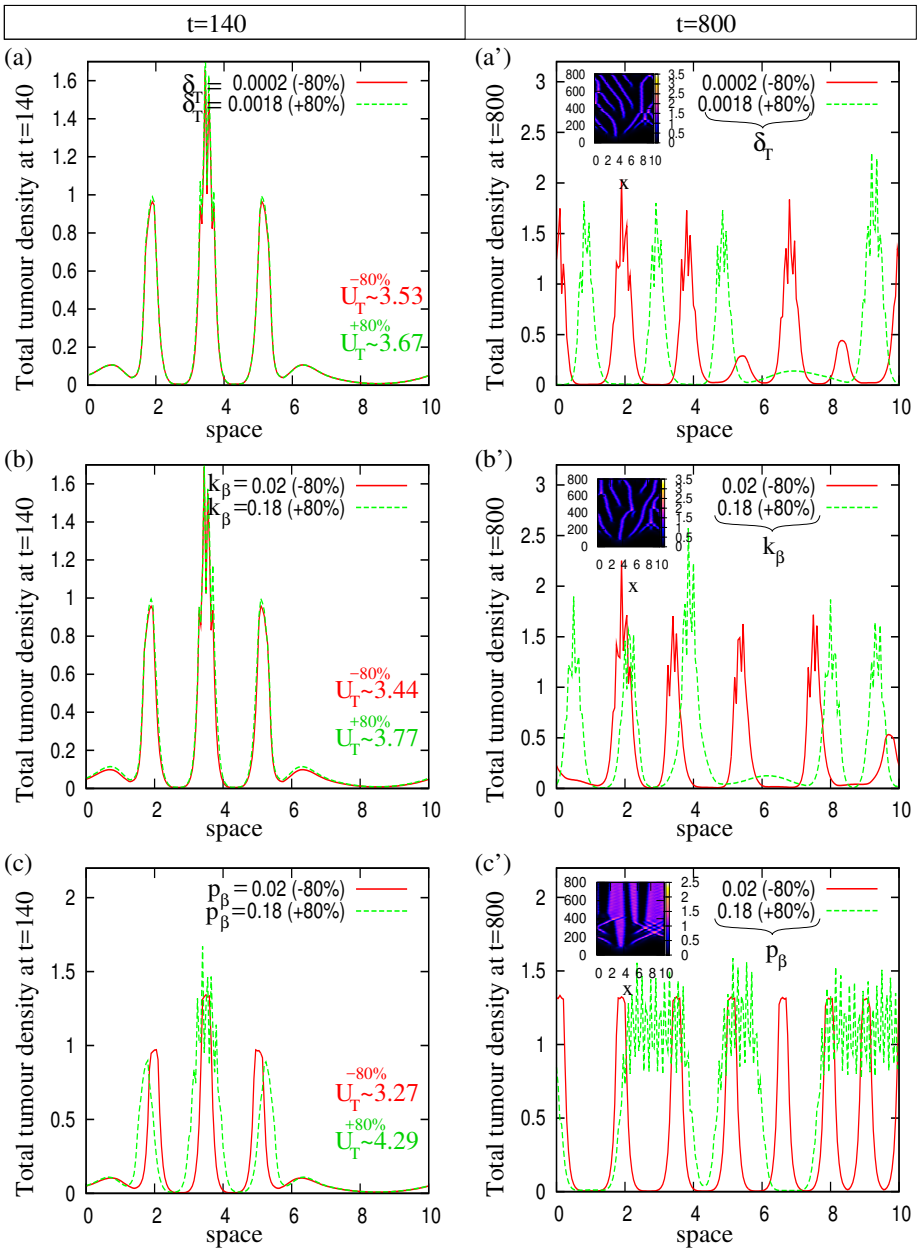

Figure 14: Tumour density $(u_T^+ + u_T^-)$ as we vary three parameters associated with TGF-β (δ_T, k_β, p_β) by $\pm 80\%$ (see values in Table 1). Initial conditions are step functions. Panels (a), (b), (c) show the spatial distribution of tumour cells at time $t = 140$. We also show here the total density of tumour cells, calculated using the formula: $U_T = (1/L)\int_0^L (u_T^+(x, 140) + u_T^-(x, 140))dx$. Panels (a'),(b'),(c') show the spatial distribution of tumour cells at time $t = 800$ days. Here we considered $q_a = 20$, $q_r = 10$, $p_T = 0.04$ and all other parameters as in Tables 1 and 2. The inset figures show space-time tumour densities corresponding to +80% changes in parameter values.

various hypotheses regarding the factors that might influence the evolution and structure of tumours in response to TGF-β cytokines.

With the help of numerical simulations, we showed that this model can explain the formation of aggregations of tumour cells (resembling tumour metastases) at positions in space further away from the main tumour aggregation (due to the TGF-β molecules that can break the adhesive bonds between the cancer cells, combined with cancer proliferation). While the asymptotic dynamics of the model was described by classical solutions with $\mathbf{O}(2)$ symmetry, such as stationary pulses (i.e., stationary cell aggregations) and rotating waves (i.e., travelling cell aggregations), the transient dynamics was puzzling. The formation of new cell aggregations at distant position in space followed by their merging with other aggregations was likely the result of spatially heterogeneous solutions which were saddle points (see the discussion in [34] on unstable steady states with exponentially small eigenvalues, i.e., metastable states, and their role on the emergence and merging of patterns). We believe that the diffusion of TGF-β and the nonlocal interactions between cells do not allow the aggregation patterns to be completely independent, leading to unstable heterogeneous patterns. However, given the nonlocal nature of model (1), investigating the stability of spatially heterogeneous solutions exhibited by this model is a difficult task, which is beyond the scope of this article. Nevertheless, an analytical investigation into the stability of heterogeneous patterns (which will be the subject of a different study) could reveal the similarities between the nonlocal hyperbolic-parabolic model (1), and other local and nonlocal models in the literature, which exhibit similar patterns. For example, similar splitting/merging aggregations have been observed in local models of parabolic type describing chemotactic behaviour of cells [42, 34], or in nonlocal parabolic models for collective movement in cells [43]. In contrast to the models in [42, 43], where splitting/merging aggregations seem to be a persistent phenomenon, in our study it is a transient phenomenon.

Some clinical studies associated larger tumour sizes (at detection time) with increased metastatic potential [35, 36, 37, 39]. Using this mathematical model, we showed that this behaviour might be the result of an increased production of TGF-β cytokine (i.e., increased p_β).

Other clinical studies associated increased tumour proliferation with increased metastasis [44, 45]. In our theoretical study, we showed distinct metastasis-like patterns for low tumour proliferation rates. We hypothesise that these metastasis-like patterns are the result of the delicate balance between the tumour growth rate, the speed of tumour cells, and the long-range effect of TGF-β molecules on cell-cell adhesion. We believe that similar patterns could be obtained also for higher proliferation rates, but given the very large parameter space (even after model non-dimensionalisation - not shown here), we did not investigate this particular aspect. The goal of this study was not to investigate the exact parameter values for which metastasis behaviours can be obtained. Rather, we wanted to show that the nonlocal effects of TGF-β molecules on cell-cell adhesion can explain the movement of cells at distant positions in space, and the formation of new cell aggregations.

Future research directions. In addition to a more detailed investigation of the short-time dynamics of model (1) that we mentioned before, there are a few more other research directions that should be investigated. From a biological point of view, it will be interesting to incorporate in model (1) the molecular mechanisms that control the TGF-β paradox, namely the switch form tumour-suppressing to tumour-promoting functions. From a mathematical point of view, it would be interesting to compare in terms of bifurcation and symmetry the dynamics of the 1D model (1) and the 2D model (25) described in Appendix B.

Acknowledgements. R.E. acknowledges partial support from an Engineering and Physical Sciences Research Council (UK) First Grant number EP/K033689/1.

Appendix A

Table 2 summarises the parameters used for the numerical simulations. For simplicity, we rescaled the density of tumour cells ($u_T^{\pm}$) by their carrying capacity, and thus for the simulations we used $K_T = 1$. This also led to a re-scaling by K_T of $q_{r,a}$, p_β and δ_T, parameters not known from the literature.

In regard to the parameters estimated/available from the literature, we note that tumour cells can migrate in a streaming mode at speeds of $1-2\mu$m/min [46]. Here, we assume that $\gamma = 1\mu$m/min=0.06mm/hr. For the tumour proliferation rate, we focus on murine B16 melanoma cells, which have a doubling time between 14-24 hours, depending on the cell line [47]. Here we consider an average of 17 hours (corresponding to B16F10 cells), which translates into a proliferation rate of $p_T = 0.04$/hr. For TGF-β parameters we note that while the active form of TGF-β has a very short half life (of 2-3 minutes), the latent form of TGF-β has a much longer half-life, of more than 100 minutes [52]. Moreover, the TGF-β half-life can be prolonged even more (to almost 159 hours) following fusion with longer-lived proteins such as antibodies [53]. Therefore, here we consider a half-life of about 6 hours, corresponding to $\delta_\beta \approx 0.11/hr$. Since total serum TGF-$\beta$ levels in control mice are varying between $8 \times 10^5 pg/ml = 0.8\mu g/ml$ [51] and $125ng/ml = 0.125\mu g/ml$ [54] (with active TGF-β levels even lower, around $10^2 pg/ml = 10^{-4}\mu g/ml$), in this theoretical study we choose $p_e = 0.1/hr/(\mu g/ml)$. For simplicity, we also approximate $p_\beta = 0.1$/hr.

In regard to the diffusion coefficient D, various studies reported different bio-molecular diffusion coefficients, depending on the substrate [48, 49]. For example, [49] reported that the diffusion coefficient of another cytokine, IL-2, can vary between 100 $\mu m^2/s$=0.36 mm^2/hr and 16 $\mu m^2/s$=0.057 mm^2/hr. However, since [50] showed that long-range diffusion is not a property of the TGF-β cytokines, throughout this study we assume a lower diffusion coefficient $D \approx 10^{-4} mm^2/hr$.

In regard to the random and directed turning rates we assume that $\lambda_1, \lambda_2 \in (0.1, 0.9)$ (since they can be interpreted as probabilities of turning per unit time; see [28]). Because we are interested in studying directed collective movement we also assume that $\lambda_1 < \lambda_2$. For simplicity, throughout this study we choose $\lambda_1 = 0.2$ and $\lambda_2 = 0.8$.

Param.	Value	Units	Description
γ	0.06	$\frac{mm}{hr}$	average speed of tumour cells [46]
λ_1	0.2 (0.1-0.9)	$\frac{1}{hr}$	approximation of the random turning rate for tumour cells
λ_2	0.8 (0.1-0.9)	$\frac{1}{hr}$	approximation of the directed turning rate for tumour cells
q_a	0–10^2	$\frac{\mu g}{cell}$	max. magnitude of attractive interactions between cells within the attraction range, in the presence of TGF-β molecules
q_r	10^1	$\frac{ml}{cell}$	magnitude of repulsive interactions between cells within repulsion range
s_a	0.3	mm	parameter that controls the spatial range of attractive cell-cell interactions
s_r	0.1 (0.01-0.1)	mm	parameter that controls the spatial range of repulsive cell-cell interactions
k_β	0.1 (0.02-0.2)	$\frac{\mu g}{ml}$	half-concentration of TGF-β necessary to decrease expression of E-cadherin and reduce cell-cell adhesion
m_0	2	–	threshold parameter that ensures that $f \approx 0$ when $y_r^{\pm} \approx y_a^{\pm}$
p_T	10^{-2}–10^{-1}	$\frac{1}{hr}$	proliferation rate of tumour cells (we assume a doubling time between 1-15 days) [47]
K_T	1	–	carrying capacity of tumour cells
K_T^*	$K_T/10^2$	–	tumour size threshold that causes TGF-β to shift from tumour-suppressing to tumour-promoting
δ_T	10^{-3} (10^{-4} – 2×10^{-3})	$\frac{\mu g}{hr \cdot cell}$	rate of tumour inhibition/growth in the presence of TGF-β molecules
D	10^{-4}	$\frac{mm^2}{hr}$	diffusion rate of TGF-β molecules [48, 49, 50]
p_e	0.1	$\frac{\mu g/ml}{hr}$	baseline rate at which TGF-β is produced by epithelial and other cells [51]
p_β	0.1 (0.02-0.2)	$\frac{1}{hr}$	rate at which TGF-β is produced by tumour cells
δ_β	0.11	$\frac{1}{hr}$	decay rate of TGF-β molecules [52, 53]
L	10	mm	domain length

Table 2: Description of model parameters and their values used during simulations. For the nonlocal interactions, we use the translated Gaussian kernels shown in Fig. 3(b). We define cells density as cell numbers per ml of blood (for mice, blood volume is about 1.5-2.5ml), and the concentration of TGF-β as $\mu g/ml$.

In regard to cell sizes, the largest cells in the body (e.g., egg cells or muscle fiber cells) can reach up to $100 - 120\mu m$ in diameter [55]. However, one of the most known cancer cell, namely the HeLa cell,

can spread on a microscope slide up to a diameter of $\approx 40/\mu m$, and when in an aggregation these cells can press on each other to compact the diameter to $\approx 20\mu m$ [25, 26]. For this reason, we chose the spatial range for cell-cell repulsion to be $s_r \in (10, 100)\mu m = (0.01, 0.1)mm$ (in Figure 3 we show $s_r = 0.05mm$). For the spatial range of cell-cell attraction, experimental studies have shown that the traction forces between cells during collective movement can extend across very large spatial distances, involving multiple cell rows [56]. In this study we assume that $s_a = 0.3mm$ (=300μm). Finally, we choose a domain of size $L = 10\,mm$ (=$10^4\,\mu m$). All other parameters listed in Table 2 are varied within the shown estimated ranges.

We emphasise that this approach (of combining parameters taken from the literature, with parameters approximated based on published experimental results, and parameters estimated within some ranges) is very common in the mathematical literature on cell biology and immunology, due to a lack of quantitative results regarding the cell responses. In addition to the fact that very few labs measure and estimate kinetic cell parameters, there is also the difficulty of interpreting kinetic data; see the review in [57]. Moreover, the few rigorously estimated kinetic parameters in the mathematical literature depend on the estimation method used, as emphasised in [58]. A more detailed discussion on model validation and parameter estimation in mathematical biology can be found in [59].

Based on these facts, we acknowledge that the majority of models in the mathematical cell biology and immunology literature, including this particular study, can have at this moment only a theoretical value. In particular, the model presented here can only propose hypotheses regarding the possible outcomes of the interactions between the TGF-β and the tumour cells.

Appendix B

For completeness, we describe a 2D version of the 1D model (1). To this end, we define $u_T(\mathbf{x}, t, \phi)$ to be the density of tumour cells at position $\mathbf{x} = (x, y)$, time t and orientation ϕ, and $u_\beta(\mathbf{x}, t)$ to be the concentration of TGF-β molecules at position $\mathbf{x} = (x, y)$ and time t. The 2D model is

$$\begin{aligned}\frac{\partial u_T(\mathbf{x},t,\phi)}{\partial t} + \gamma e_\phi \nabla_{\mathbf{x}} u_T(\mathbf{x},t,\phi) =& -\lambda[u_T(\mathbf{x},t,\phi)]u_T(\mathbf{x},t,\phi) \\ &+ \int_{-\pi}^{\pi} \mathcal{T}(\mathbf{x},t,\phi,\phi')u_T(\mathbf{x},t,\phi')d\phi' \\ &+ R[u_T, u_\beta], \qquad (25a)\\ \frac{\partial u_\beta(\mathbf{x},t)}{\partial t} =& D\Delta_{\mathbf{x}} u_\beta(\mathbf{x},t) + p_e + p_\beta \int_{-\pi}^{\pi} u_T(\mathbf{x},t,\phi)d\phi \\ &- \delta_\beta u_\beta(\mathbf{x},t). \qquad (25b)\end{aligned}$$

The velocity of cells moving in direction ϕ is $\gamma e_\phi = \gamma(\cos(\phi), \sin(\phi))$. The reaction term $R[u_T, u_\beta]$ is similar to the one in (1), but the carrying capacity is determined by all tumour cells moving in all possible directions ϕ:

$$\begin{aligned} R[u_t(\mathbf{x},t,\phi), u_\beta(\mathbf{x},t)] &= \frac{1}{2} p_T u_T \Big(1 - \frac{\int_{-\pi}^{\pi} u_T(\mathbf{x},t,\phi)d\phi}{K_T}\Big) \\ &\quad -\delta_T u_T u_\beta \Big(\tilde{K}_T - \int_{-\pi}^{\pi} u_T(\mathbf{x},t,\phi)d\phi\Big). \end{aligned} \tag{26}$$

The term $\lambda[u_T]$ describes the turning of individuals at $(\mathbf{x}, t)$ out of direction ϕ, while the nonlocal term $\int_{-\pi}^{\pi} \mathcal{T}(\mathbf{x},t,\phi,\phi')d\phi'$ describes the turning into direction ϕ, from all possible directions $\phi' \in [-\pi, \pi]$. These two operators that define the turning behaviour depend on nonlocal attractive-repulsive interactions between cells:

$$\begin{aligned} \lambda[u_T(\mathbf{x},t,\phi)] = \quad & q_r \int_{\mathbb{R}^2} \int_{-\pi}^{\pi} K_r^d(\mathbf{x}-\mathbf{s}) K_r^o(\mathbf{s};\mathbf{x},\phi) u_T(\mathbf{s},t,\theta) d\theta d\mathbf{s} \\ & + q_a \int_{\mathbb{R}^2} \int_{-\pi}^{\pi} K_a^d(\mathbf{x}-\mathbf{s}) K_a^o(\mathbf{s};\mathbf{x},\phi) \tfrac{u_T(\mathbf{s},t,\theta)}{k_\beta + u_\beta(\mathbf{s},t)} d\theta d\mathbf{s}, \end{aligned} \tag{27}$$

and

$$\begin{aligned} &\mathcal{T}(\mathbf{x},t,\phi,\phi') = \\ &q_r \int_{\mathbb{R}^2} \int_{-\pi}^{\pi} K_r^d(\mathbf{x}-\mathbf{s}) K_r^o(\mathbf{s};\mathbf{x},\phi') W_r(\phi'-\phi, \phi'-\psi) u_T(\mathbf{s},t,\theta) d\theta ds \\ &+ q_a \int_{\mathbb{R}^2} \int_{-\pi}^{\pi} K_a^d(\mathbf{x}-\mathbf{s}) K_a^o(\mathbf{s};\mathbf{x},\phi') W_a(\phi'-\phi, \phi'-\psi) \frac{u_T(\mathbf{s},t,\theta)}{k_\beta + u_\beta} d\theta ds \end{aligned} \tag{28}$$

The spatial kernels $K_{r,a}^d$ and orientational kernels $K_{r,a}^o$ can be defined as in [60]:

$$K_j^d(\mathbf{x}) = \frac{1}{A_j} e^{-(\sqrt{x^2+y^2} - d_j)^2 / m_j^2}, \ j = r, a, \tag{29}$$

$$\begin{aligned} K_j^o(\mathbf{s};\mathbf{x},t) &= \frac{1}{2\pi}\Big(1 \pm \cos(\phi - \psi)\Big), \ \ j = r, a, \ (\text{“}+\text{”} \text{for } j = r; \ \text{“}-\text{”} \text{for } j = a), \\ &= \frac{1}{2\pi}\Big(1 \pm \cos(\phi)\frac{s_x}{\sqrt{s_x^2 + s_y^2}} \pm \sin(\phi)\frac{s_y}{\sqrt{s_x^2 + s_y^2}}\Big) \end{aligned} \tag{30}$$

with d_r and d_a describing the repulsive and attractive spatial interaction ranges, $m_{r,a}$ describing the width of these ranges, and $A_{r,a}$ constants that ensure that each kernel integrates to 1 [60]. The angle ψ that appears in (27)-(28) is the angle formed by the direction of $\mathbf{x} - \mathbf{s}$ with the positive x-axis (see Fig. 15). Finally, function $W_{r,a}$ describes the probability that cells change direction from ϕ' to ϕ upon interactions with other cells positioned at $\mathbf{s}$ (within the repulsive “r” and attractive “a” spatial ranges), which are having direction θ. $W_{r,a}$ must satisfy $\int_{-\pi}^{\pi} W_{r,a}(\phi'-\phi, \phi'-\psi)d\phi$=1. An example of such function is given in [60], where $W(\phi'-\phi, \phi'-\psi) = 1/2\sigma$ if $|\phi'-\phi-v(\phi'-\psi)| < \sigma$ and $W(\phi'-\phi, \phi'-\psi) = 0$ if $\sigma < |\phi'-\phi-v(\phi'-\psi)| \leq \pi$, with the turning function $v(\Theta) = k\Theta$, $-1 \leq k \leq 1$. Note that, as in [60], the previous assumptions lead to

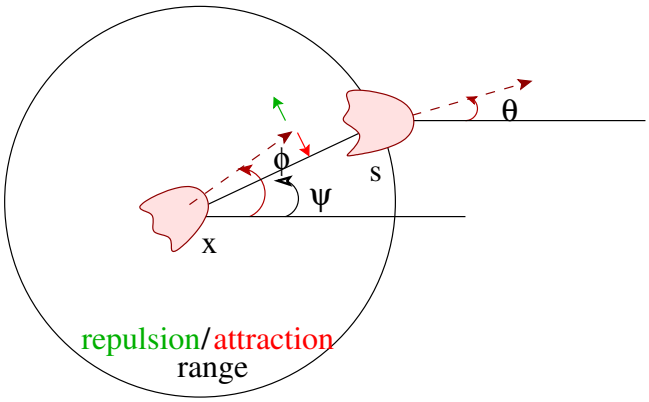

Figure 15: Cell re-orientation in 2D. The reference cell at x, moving in direction ϕ, will change its direction towards/away the position s of neighbouring cells within the attraction/repulsion ranges of interaction. We assume that these neighbouring cells at s have orientation $\theta \in (-\pi, \pi]$. We denote by ψ the angle made by the vector $\mathbf{x} - \mathbf{s}$ and the positive x-axis.

$$\lambda(\mathbf{x}, \phi) = \int_{-\pi}^{\pi} T(\mathbf{x}, \phi, \phi')d\phi',$$

and thus the turning rate from direction ϕ into any other direction is obtained by integrating the re-orientation term $T(\mathbf{x}, \phi, \phi')$ over all possible directions ϕ'. However, model (25) cannot be reduced to the the 1D model (1), since the turning behaviour of u_T cells is now linear, as opposed to the nonlinear turning rates (3) in the 1D model. If we would assume nonlinear turning also for the 2D model, namely $\lambda[u_T(\mathbf{x}, t, \phi)] = f[u_T(\mathbf{x}, t, \phi)]$ with $f[y] = 0.5{+}0.5\tanh(K{*}y)$ and $T(\mathbf{x}, t, \phi, \phi') = f[u_T(\mathbf{x}, t, \phi), u_T(\mathbf{x}, t, \phi'), u_\beta(\mathbf{x}, t)]$, then we could not connect anymore the turning terms λ and T.

We emphasise that the aim of this paper is not to investigate the dynamics of the 2D model (which, due to model differences, we believe it will be slightly different from the dynamics of the 1D model). This will be the subject of a future study, which will focus on a symmetry and bifurcation investigation of the patterns described by these 1D and 2D models (with linear turning behaviour, i.e., $f(y) = y$). Rather, the goal of this paper was to show that the effect of TGF-β on cell-cell adhesive interactions could explain the observed tumour metastasis patterns.

Appendix C

In the following we prove the stability result in Proposition 3.3. First, we note that when $u_T^{*,+} = u_T^{*,-}$, the following terms that appear in the dispersion relation (19) are equal: $A_1 = A_2$, $B_1^\beta = B_2^\beta$, $B_1^+ = B_2^-$ and $B_1^- = B_2^+$. Moreover, for $q_a = q_r = 0$, the coefficients A, B and C in the dispersion relation are all real. Therefore, the roots of the cubic polynomial

$$\sigma^2 + A\sigma^2 + B\sigma + C = 0$$

are all negative provided that the following Routh-Hurwitz stability conditions hold:

$$A > 0, \quad C > 0, \quad B > 0, \quad \text{and} \quad AB > C.$$

In the following, we will show that each of these inequalities hold provided that the conditions in the statement of Proposition 3.3 are valid.

"$\mathbf{A > 0}$". We use the equation for the steady state u_T^*, namely $p_T(1-u_T^*/K_T) = \delta_T u_\beta^*(\tilde{K}_T - u_T^*)$, to re-write the expression for A:

$$A = \big[(Dk^2 + \delta_\beta) + 2\big(\lambda_1 + \lambda_2 f(0)\big)\big] + p_T - \delta_T u_T^* u_\beta^*.$$

Since the first term is positive, we have $A > 0$ if the following condition holds: $p_T > \delta_T u_T^* u_\beta^*$.

"$\mathbf{C > 0}$". Since $Dk^2 + \delta_\beta \geq \delta_\beta$ we have

$$\begin{aligned} C &\geq \delta_\beta (B_1^+ - B_1^-)(B_1^+ + B_1^-) - 2p_\beta B_1^\beta (B_1^- - B_1^+) \\ &= (B_1^- - B_1^+)\big[-\delta_\beta (B_1^+ + B_1^-) - 2p_\beta B_1^\beta \big]. \end{aligned}$$

If condition (21c) holds true then $B_1^- - B_1^+ = 2(\lambda_1 + \lambda_2 f(0)) + p_T(1 - u_T^*/K_T) > 0$. Therefore $C > 0$ reduces to showing that the second term is positive.

$$-\delta_\beta (B_1^+ + B_1^-) - 2p_\beta B_1^\beta \quad = \quad u_T^* \big[\delta_\beta (\frac{p_T}{K_T} - \delta_T u_\beta^*) + p_\beta \delta_T (K_T^* - u_T^*)\big] > 0$$

provided that condition (21d) holds true.

"$\mathbf{AB > C}$". First, we note that if $p_T > \delta_T u_T^* u_\beta^*$ then $B_1^+ < 0$ since

$$B_1^+ = -\Big[\frac{p_T}{2} - \frac{\delta_T}{2} u_T^* u_\beta^*\Big] - \big[\lambda_1 + \lambda_2 f(0)\big] < 0.$$

Since AB and C have a common term $((Dk^2 + \delta_\beta) \cdot (\gamma^2 k^2 + (B_1^+)^2 - (B_1^-)^2))$, showing that $AB > C$ reduces to showing that

$$\begin{aligned} \big[(Dk^2 + \delta_\beta) 2B_1^+ - 2p_\beta B_1^\beta\big][Dk^2 + \delta_\beta - 2B_1^+] \quad &+ \quad 2B_1^+ \big[\gamma^2 k^2 + (B_1^+)^2 - (B_1^-)^2\big] \\ &< \quad p_\beta 2B_1^\beta (B_1^- - B_1^+). \end{aligned}$$

Note that, assuming $u_T^* > K_T > K_T^*$, we obtain $B_1^\beta > 0$. Then the right-hand-side of the previous inequality is

$$\begin{aligned} p_\beta 2B_1^\beta (B_1^- - B_1^+) \quad &= \quad 2p_\beta B_1^\beta \big[2(\lambda_1 + \lambda_2 f(0)) + \delta_T u_\beta^* (K_T^* - u_T^*)\big] \\ &= \quad 2p_\beta B_1^\beta \big[2(\lambda_1 + \lambda_2 f(0)) + p_T\big(1 - \frac{u_T^*}{K_T}\big)\big] > 0 \end{aligned}$$

provided that $2(\lambda_1+\lambda_2 f(0))+p_T\big(1-u_T^*/K_T\big) > 0$. For the left-hand-side terms, since $B_1^+ < 0$ we have $Dk^2+\delta_\beta-2B_1^+ > 0$ and $(Dk^2+\delta_\beta)2B_1^+ - 2p_\beta B_1^\beta < 0$. Finally,

$$
\begin{aligned}
&2B_1^+\big[\gamma^2k^2+(B_1^+)^2-(B_1^-)^2\big] = 2B_1^+\big[\gamma^2k^2+(B_1^+-B_1^-)(B_1^++B_1^-)\big]\\
&= 2B_1^+\gamma^2k^2 - 2B_1^+\Big[2(\lambda_1+\lambda_2 f(0))+p_T(1-\frac{u_T^*}{K_T})\Big]\Big[2A_1-\delta_T u_\beta^*(K_T^*-u_T^*)\Big]\\
&= 2B_1^+\gamma^2k^2 - 2B_1^+\Big[2(\lambda_1+\lambda_2 f(0))+p_T(1-\frac{u_T^*}{K_T})\Big]\Big[-\frac{p_T}{K_T}u_T^*+\delta_T u_T^* u_\beta^*\Big] < 0
\end{aligned}
$$

provided that conditions (21a) and (21c) in the statement of Proposition 3.3 hold. In particular, we use the fact that $p_T > \delta_T u_T^* u_\beta^*$ is equivalent to

$$-\frac{p_T}{K_T}u_T^*+\delta_T u_T^* u_\beta^* < 0$$

Therefore $AB > C$.

"$\mathbf{B} > \mathbf{0}$". Since $A > 0$, $C > 0$ and $AB > C$ we have that $B > 0$.

All conditions in the Routh-Hurwitz stability criterion are satisfied, and thus the real parts of all roots of the dispersion relation (19) are negative, which ensures the stability of the non-zero state with $\mathbf{O}(2)$ symmetry for the case $q_a = q_r = 0$.

References

[1] S. Paget, The distribution of secondary growths in cancer of the breast, Lancet 133 (3421) (1889) 571–573.

[2] D. Hanahan, R. Weinberg, The hallmarks of cancer, Cell 100 (2000) 57–70.

[3] D. Hanahan, R. Weinberg, Hallmarks of cancer: the next generation, Cell 144 (2011) 646–674.

[4] M. Blanco, Y. Kang, Signalling pathways in breast cancer metastasis - novel insights from functional genomics, Breast Cancer Res. 13 (2) (2011) 206.

[5] L. Rosen, H. Ashurst, L. Chap, Targeting signal transduction pathways in metastatic breast cancer: a comprehensive review, The Oncologist 15 (2010) 216–235.

[6] X. Guo, X. Wang, Signalling cross-talk between TGF-β/BMP and other pathways, Cell Research 19 (2009) 71–88.

[7] D. Padua, J. Massagué, Roles of TGFβ in metastasis, Cell Research 19 (2009) 89–102.

[8] D. Principe, J. Doll, B. Jung, H. Munshi, L. Bartholin, B. Pasche, C. Lee, P. Grippo, TGF-β: Duality of function between tumour prevention and carcinogenesis, JNCI J. Natl. Cancer Inst. 106 (2) (2014) djt369.

[9] N. Dumont, C. Artega, Targeting the TGFβ signalling network in human neoplasia, Cancer Cell 3 (2003) 531–546.

[10] A. Moustakas, C. Heldin, Signalling networks guiding epithelial-mesenchimal transitions during embryogenesis and cancer progression, Cancer Sci. 98 (2007) 1512–1520.

[11] C. Neuzilleta, A. Tijeras-Raballandb, R. Cohenb, J. Crosc, S. Faivrea, E. Raymondd, A. de Gramont, Targeting the TGF-β pathway for cancer therapy, Pharmacology & Therapeutics 147 (2015) 22–31.

[12] T. Gohongi, D. Fukumura, Y. Boucher, C. Yun, G. Soff, C. Compton, T. Todoroki, R. Jain, Tumor-host interactions in the gallbladder suppress distal angiogenesis and tumor growth: involvement of transforming growth factor β1, Nat. Med. 5 (1999) 1203–1208.

[13] P. Melke, H. Jonsson, E. Pardali, P. ten Dijke, C. Peterson, A rate equation approach to elucidate the kinetics and robustness of the TGF-beta pathway, Biophys. J. 91 (2006) 4368–4380.

[14] S. Chung, F. Miles, R. Sikes, C. Cooper, M. Farach-Carson, B. Ogunnaike, Quantitative modelling and analysis of the transforming growth factor β signalling pathway, Biophysical Journal 96 (2009) 1733–1750.

[15] Z. Zi, D. Chapnick, X. Liu, Dynamics of TGF-β/Smad signalling, FEBS Letters 586 (14) (2012) 1921–1928.

[16] G. Ascolani, P. Liò, Modelling TGF-β in early stages of cancer tissue dynamics, PLoS One 9 (2) (2014) e88533.

[17] J. Arciero, T. Jackson, D. Kirschner, A mathematical model of tumor-immune evasion and siRNA treatment, Discrete and Continuous Dynamical Systems B 4 (1) (2004) 39–58.

[18] Y. Kim, H. Othmer, A hybrid model of tumor-stromal interactions in breast cancer, Bull. Math. Biol. 75 (2013) 1304–1350.

[19] S. Wang, P. Hinow, N. Bryce, A. Weaver, L. Estrada, C. Arteaga, G. Webb, A mathematical model quantifies proliferation and motility effects of TGF-β on cancer cells, Comput. Math. Methods Med. 10 (1) (2009) 71–83.

[20] S. Goswami, E. Sahai, J. Wyckoff, M. Cammer, D. Cox, F. Pixley, E. Stanley, J. Segall, J. Condeelis, Macrophages promote the invasion of breast carcionma cells via a colony-stimulating factor-1/epidermal growth factor paracrine loop, Cancer Res. 65 (12) (2005) 5278–5283.

[21] S. Hirohashi, Y. Kanai, Cell adhesion system and human cancer morphogenesis, Cancer Sci. 94 (2003) 575–581.

[22] J. Batson, L. MacCarthy-Morrogh, A. Archer, H. Tanton, C. Nobes, EphA receptors regulate prostate cancer cell dissemination through Vav2-RhoA mediated cell-dell repulsion, Biology Open (2014) 1–10.

[23] C. Reinhart-King, M. Dembo, D. Hammer, Cell-cell mechanical communication through compliant substrates, Biophysical Journal 95 (2008) 6044–6051.

[24] R. Fetecau, R. Eftimie, An investigation of a nonlocal hyperbolic model for self-organization of biological groups, J. Math. Biol. 61 (4) (2010) 545–579.

[25] T. Puck, P. Marcus, S. Cieciura, Clonal growth of mammalian cells in vitro; growth characteristics of colonies from single HeLa cells with and without a "feeder" layer, J. Exp. Med. 103 (2) (1956) 273–284.

[26] A. Luciani, A. Rosi, P. Matarrese, G. Arancia, L. Guidoni, V. Viti, Changes in cell volume and internal sodium concentration in HeLa cells during exponential growth and following Ionidamine treatment, European J. Cell Biol. 80 (2) (2001) 187–195.

[27] K. Hadeler, Reaction transport systems in biological modelling, Mathematical and computer modelling 31 (4-5) (2000) 75–81.

[28] R. Eftimie, Hyperbolic and kinetic models for self-organised biological aggregations and movement: a brief review, J. Math. Biol. 65 (1) (2012) 35–75.

[29] O. Sacco, D. Romberger, A. Rizzino, J. Beckmann, S. Rennard, J. Spurzem, Spontaneous production of transforming growth factor -β2 by primary cultures of bronchial epithelial cells. effects on cell behaviour in vitro., J. Clin. Invest. 90 (1992) 1379–1385.

[30] G. Grotendorst, G. Smale, D. Pencev, Production of transforming growth factor beta by human peripheral blood monocytes and neutrophils, J. Cell Physiol. 140 (2) (1989) 396–402.

[31] R. Eftimie, G. de Vries, M. Lewis, F. Lutscher, Modelling group formation and activity patterns in self-organising collectives of individuals, Bull. Math. Biol. 69 (5) (2007) 1537–1565.

[32] M. Golubitsky, I. Stewart, D. Schaeffer, Singularities and groups in bifurcation theory. Vol. II, Springer, 2000.

[33] P.-L. Buono, R. Eftimie, Codimension-2 bifurcations in animal aggregation models with symmetry, SIAM J. on Appl. Dyn. Syst. 13 (4) (2014) 1542–1582.

[34] A. Potapov, T. Hillen, Metastability in chemotaxis models, Journal of Dynamics and Differential Equations 17 (2) (2005) 293–330.

[35] S. Koscielny, M. Tubiana, M. Lê, A. Valleron, H. Mouriesse, G. Contesso, D. Sarrazin, Breast cancer: relationship between the size of the primary tumour and the probability of metastatic dissemination, Br. J. Cancer 49 (1984) 709–715.

[36] A. Minn, G. Gupta, D. Padua, P. Bos, D. Nguyen, D. Nuyten, B. Kreike, Y. Zhang, Y. Wang, H. Ishwaran, J. Foekens, M. van de Vijver, J. Massagué, Lung metastasis genes couple breast tumour size and metastatic spread, Proc. Natl. Acad. Sci. USA 104 (2007) 6740–6745.

[37] T. Klatte, J.-J. Patard, M. D. Marino, K. Bensalah, G. Verhoest, A. de Taille, C.-C. Abbou, E. Allhoff, G. Carrieri, S. Riggs, F. Kabbinavar, A. Belldegrun, A. Pantuck, Tumour size does not predict risk of metastatic disease or prognostic of small renal cell carcinomas, The Journal of Urology 179 (2008) 1719–1726.

[38] M. Kates, R.Korets, N. Sadeghi, P. Pierorazio, J. McKiernan, Predictors of locally advanced and metastatic disease in patients with small renal masses, BJU International 109 (2012) 1463–1467.

[39] J. Ingimarsson, M. Sigurdsson, S. Hardarson, V. Petursdottir, E. Jonsson, G. Einarsson, T. Gudbjartsson, The impact of tumour size on the probability of synchronous metastasis and survival in renal cell carcinoma patients: a population-based study, BMC Urology 14 (2014) 72.

[40] M. Nguyen, I. Gill, Effect of renal cancer size on the prevalence of metastasis at diagnosis and mortality, The Journal of Urology 181 (2009) 1020–1027.

[41] J. Tse, G. Cheng, J. Tyrrell, S. Wilcox-Adelman, Y. Boucher, R. Jain, L. Munn, Mechanical compression drives cancer cells toward invasive phenotype, Proc. Natl. Acad. Sci. USA 109 (3) (2012) 911–916.

[42] K. Painter, T. Hillen, Spatio-temporal chaos in a chemotaxis model, Physica D 240 (2011) 363–375.

[43] K. Painter, J. Bloomfield, J. Sherratt, A. Gerisch, A nonlocal model for contact attraction and repulsion in heterogeneous cell populations, Bull. Math. Biol. 77 (6) (2015) 1132–1165.

[44] O.-P. Kallioniemi, K. Holli, T. Visakorpi, T. Koivula, H. Helin, J. Isola, Association of C-*erb*B-2 protein over-expression with high rate of cell proliferation, increased risk of visceral metastasis and poor long-term survival in breast cancer, International Journal of Cancer 49 (5) (1991) 650–655.

[45] Y. Takahashi, Y. Kitadi, C. Bucana, K. Cleary, L. Ellis, Expression of vascular endothelial growth factor and its receptor, KDR, correlates with vascularity, metastasis, and proliferation of human colon cancer, Cancer Res. 55 (1995) 3964–3968.

[46] A. Clark, D.M.Vignjevic, Modes of cancer cell invasion and the role of the microenvironment, Current Opinion in Cell Biology 36 (2015) 13–22.

[47] C. Danciu, A. Falamas, C. Dehelean, C. Soica, H. Radeke, L. Barbu-Tudoran, F. Bojin, S. Pînzaru, M. Munteanu, A characterization of four B16 murine melanoma cell sublines molecular fingerprint and proliferation behavior, Cancer Cell International 13 (2013) 75.

[48] T. Kihara, J. Ito, J. Miyake, Measurement of biomolecular diffusion in extracellular matrix condensed by fibroblasts using fluorescence correlation spectroscopy, PLoS One 8 (11) (2013) e82382.

[49] T. Höfer, O. Krichevsky, G. Altan-Bonnet, Competition for IL-2 between regulatory and effector T cells to chisel immune responses, Frontiers in Immunology 3 (2012) 268.

[50] C. Jones, N. Armes, J. Smith, Signalling by TGF-beta family members: short-range effects of Xnr-2 and BMP-4 contrast with the long-range effects of activin, Curr. Biol. 6 (11) (1996) 1468–1475.

[51] K. Shibahara, M. Ota, M. Horiguchi, K. Y. abd J. Melamed, D. Rifkin, Production of gastrointestinal tumors in mice by modulating latent Transforming Growth Factor beta 1 activation, Cancer Res. 73 (2013) 459–468.

[52] L. Wakefield, T. Winokur, R. Hollands, K. Christopherson, A. Levinson, M. Sporn, Recombinant latent transforming growth factor beta 1 has a longer plasma half-life in rats than active transforming growth factor beta 1, and a different tissue distribution, J. Clin. Invest. 86 (1990) 1976–1984.

[53] P. Hermonat, D. Li, B. Yang, J. Meha, Mechanism of action and delivery possibilities for TGFβ_1 in the treatment of myocardial ischemia, Cardiovascular Research 74 (2007) 235–243.

[54] S. Khan, J. Joyce, T. Tsuda, Quantification of active and total transforming growth factor-β levels in serum and solid organ tissues by bioassay, BMC Research Notes 5 (2012) 636.

[55] S. Patel, J. Harwig, J. J. Italiano, The biogenesis of platelets from megakaryocyte proplatelets, J. Clin. Invest. 115 (12) (2005) 3348–3354.

[56] X. Trepat, M. Wasserman, T. Angelini, E. Millet, D. Weitz, J. Butler, J. Fredberg, Physical forces during collective cell migration, Nature Physics 5 (2009) 426–430.

[57] R. D. Boer, A. Perelson, Quantifying T lymphocyte turnover, J. Theor. Biol. 327 (2013) 45–87.

[58] D. Laydon, C. Bangham, B. Asquith, Estimating T-cell repertoire diversity: limitations of classical estimators and a new approach, Philos. Trans. R. Soc. Lond. B Biol. Sci. 370 (1675) (2015) 20140291.

[59] R. Eftimie, J. Gillard, D. Cantrell, Mathematical models for immunology: current state of the art and future research directions, Bull. Math. Biol. 78 (10) (2016) 2091–2134.

[60] R. Fetecau, Collective behaviour of biological aggregations in two dimensions: a nonlocal kinetic model, Math. Models Methods Appl. Sci. 21 (7) (2011) 1539–1569.